Chapter 2
Decay and Amplification of Magnetic Fields

It's not whether a thing is hard to understand.
It's whether, once understood, it makes any sense.

Hans Zinsser
Rats, Lice and History (1934)

We now begin our long modelling journey towards astrophysical dynamos. This chapter concentrate for the most part on a series of (relatively) simple model problems illustrating the myriad of manners in which a flow and a magnetic field can interact. We first consider the purely resistive decay of magnetic fields (Sect. 2.1), then examine various circumstances under which stretching and shearing by a flow can amplify a magnetic field (Sect. 2.2). This is followed by a deeper look at some important subtleties of these processes in the context of some (relatively) simple 2D flows (Sect. 2.3). We then move on to the so-called anti-dynamo theorems (Sect. 2.4), which will shed light on results from previous sections and indicate the way towards dynamo action, which we will finally encounter in Sects. 2.5 and 2.6.

Some of the material contained in this chapter may feel pretty far removed from the realm of astrophysics at times, but please do stick to it because the physical insight (hopefully) developed in the following sections will prove essential to pretty much everything that will come next.

2.1 Resistive Decays of Magnetic Fields

Before we try to come up with flows leading to field amplification and dynamo action, we better understand the enemy, namely magnetic field decay by Ohmic dissipation. Consequently, and with the sun and stars in mind, we first consider the evolution of magnetic fields in a sphere (radius R) of electrically conducting fluid, in the absence of any fluid motion (or, more generally, in the $\mathrm{R_m} \ll 1$ limit). The induction equation then reduces to

P. Charbonneau, *Solar and Stellar Dynamos*, Saas-Fee Advanced Course 39,
DOI: 10.1007/978-3-642-32093-4_2, © Springer-Verlag Berlin Heidelberg 2013

$$\frac{\partial \boldsymbol{B}}{\partial t} = -\nabla \times (\eta \nabla \times \boldsymbol{B}) = \eta \nabla^2 \boldsymbol{B} - (\nabla \eta) \times (\nabla \times \boldsymbol{B}) \,. \tag{2.1}$$

Were it not that we are dealing here with a vector—as opposed to scalar—quantity, for constant η this would look just like a simple heat diffusion equation, with η playing the role of thermal diffusivity. Our derivation of the magnetic energy equation (1.87) already indicates that under such circumstances, the field can only decay. Back in Chap. 1 we already obtained an order-of-magnitude estimate for the timescale $\tau_\eta \sim \ell^2/\eta$ over which a magnetic field $\boldsymbol{B}$ with typical length scale ℓ can be expected to resistively decay, which in the case of the stellar interiors ended up at $\sim 10^{10}$ yr, i.e., about the main-sequence lifetime of the sun. Let's now validate this estimate by securing formal solutions to the diffusive decay problem.

2.1.1 Axisymmetric Magnetic Fields

Without any significant loss of generality, we can focus on *axisymmetric* magnetic fields, i.e., fields showing symmetry with respect to an axis, usually rotational. Working in spherical polar coordinates (r, θ, ϕ) with the polar axis coinciding with the field's symmetry axis, the most general axisymmetric (now meaning $\partial/\partial\phi = 0$) magnetic field can be written as:

$$\boxed{\boldsymbol{B}(r, \theta, t) = \nabla \times (A(r, \theta, t)\hat{\boldsymbol{e}}_\phi) + B(r, \theta, t)\hat{\boldsymbol{e}}_\phi} \,. \tag{2.2}$$

Here the vector potential component A defines the *poloidal* component of the magnetic field, i.e., the component contained in meridional (r, θ) planes. The azimuthal component B is often called the *toroidal field*. Equation (2.2) satisfies the constraint $\nabla \cdot \boldsymbol{B} = 0$ by construction, and another great advantage of this mixed representation is that the MHD induction equation for the vector $\boldsymbol{B}$ can be separated in two equations for the scalar components A and B. The trick is the following: substitution of Eq. (2.2) into (2.1) leads to a series of (vector) terms, some oriented in the (toroidal) $\hat{\boldsymbol{e}}_\phi$-direction, others perpendicularly, in the (poloidal) meridional plane. The original, full induction equation can only be satisfied if the two sub-equations defined by each sets of orthogonal terms are individually satisfied, thus defining two separate evolution equations for A and B.

In the case of pure diffusive decay, and for a magnetic diffusivity η depending at worst only on r, this poloidal/toroidal separation leads to:

$$\frac{\partial A}{\partial t} = \eta \left(\nabla^2 - \frac{1}{\varpi^2} \right) A \,, \tag{2.3}$$

$$\frac{\partial B}{\partial t} = \eta \left(\nabla^2 - \frac{1}{\varpi^2} \right) B + \frac{1}{\varpi} \frac{\partial \eta}{\partial r} \frac{\partial (\varpi B)}{\partial r} \,, \tag{2.4}$$

where $\varpi = r \sin\theta$. These are still diffusion-like PDEs, now fully decoupled from one another. In the "exterior" $r > R$ there is only vacuum, which implies vanishing electric currents. In practice we will need to match whatever solution we compute in $r < R$ to a current-free solution in $r > R$; such a solution must satisfy

$$\mu_0 \boldsymbol{J} = \nabla \times \boldsymbol{B} = 0 \,. \tag{2.5}$$

For an axisymmetric system, Eq. (2.5) translates into the requirement that

$$\left(\nabla^2 - \frac{1}{\varpi^2}\right) A(r,\theta,t) = 0 \,, \qquad r > R \,, \tag{2.6}$$

$$B(r,\theta,t) = 0 \,, \qquad r > R \,. \tag{2.7}$$

Solutions to Eq. (2.6) have the general form

$$A(r,\theta,t) = \sum_{l=1}^{\infty} a_l \left(\frac{R}{r}\right)^{l+1} Y_{l0}(\cos\theta) \qquad r > R \,, \tag{2.8}$$

where the Y_{l0} are the usual spherical harmonics of $m = 0$ azimuthal order, and l is a positive integer, modes with negative l being discarded to ensure proper behavior as $r \to \infty$.

2.1.2 Poloidal Field Decay

Let us now seek specific solutions for a few situations of solar/stellar interest.[1] The first point to note is that the coefficients that appear in Eqs. (2.3)–(2.4) have no explicit dependence on time; provided that the magnetic diffusivity η is at worst only a function of r, it is then profitable to seek a separable solution of the form:

$$e^{-\lambda t} f_\lambda(r)\, Y_{lm}(\theta,\phi) \,, \tag{2.9}$$

where the Y_{lm} are again the spherical harmonics, the natural functional basis for modal development on a spherical surface. Substitution of this Ansatz into Eq. (2.3) with $m = 0$ in view of axisymmetry, yields the ODE:

$$\left[\frac{1}{r^2}\frac{\mathrm{d}}{\mathrm{d}r} r^2 \frac{\mathrm{d}}{\mathrm{d}r} - \frac{l(l+1)}{r^2} + \frac{\lambda}{\eta(r)}\right] f_\lambda(r) = 0 \,. \tag{2.10}$$

[1] This and the following subsection are to a large extent adapted from class notes written by Thomas J. Bogdan for the graduate class APAS7500 we co-taught in 1997 at CU Boulder.

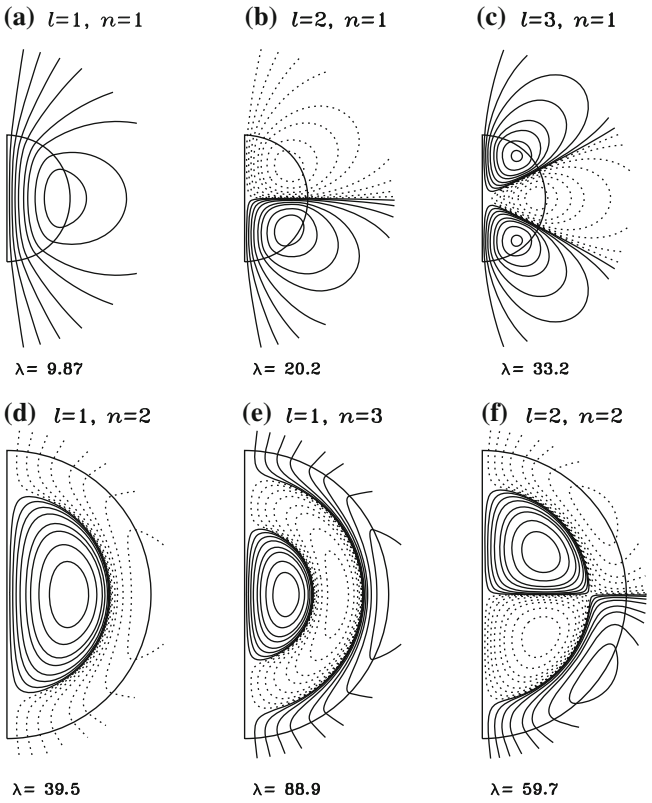

Fig. 2.1 Six diffusive eigenmodes for a purely poloidal field pervading a sphere of constant magnetic diffusivity embedded in vacuum. The *top row* shows the three fundamental ($n = 1$) diffusive eigenmodes with smallest eigenvalues, i.e., largest decay times. They correspond to the well-known dipolar, quadrupolar, and hexapolar modes ($l = 1, 2$ and 3). The *bottom row* shows a few eigenmodes of higher radial overtones. Poloidal fieldlines are shown in a meridional plane, and the eigenvalues are given in units of the inverse diffusion time ($\tau^{-1} \sim \eta/R^2$).

Assume now that the magnetic diffusivity η is constant; the spherical Bessel functions $j(kr)$, with $k^2 = \lambda/\eta$, are then the appropriate solution. The decay rate, λ, is then determined by the above 1D eigenvalue problem, along with some boundary conditions at the surface of the sphere, which turns out to depend on the vector character of the decaying magnetic field.

We first consider the decay of a purely poloidal field, i.e., $f_\lambda(r)$ is taken to describe the radial dependency of the toroidal vector potential component $A(r, \theta, t)$. Both the interior solution and outer potential field solution carry the Y_{l0} angular dependency, so continuity of A at $r = R$ demands that

$$f_\lambda(r) = \begin{cases} j_l(kr) & r < R \ , \\ j_l(kR)\left(\frac{R}{r}\right)^{l+1} & r > R \ . \end{cases} \tag{2.11}$$

The continuity of the radial derivative at $r = R$, necessary for the continuity of the latitudinal component of the magnetic field, then requires

$$kRj_l'(kR) + (l+1)j_l(kR) = kRj_{l-1}(kR) = 0 \ , \tag{2.12}$$

which means that the decay rate of a poloidal magnetic field is determined by the zeros of a spherical Bessel function. An $l = 1$ dipole calls for the positive zeros of $j_0(x) = \sin x/x$:

$$\lambda_n = \frac{\eta\pi^2 n^2}{R^2} \qquad \text{for } l = 1 \ , \ n = 1, 2, 3, \ldots \ . \tag{2.13}$$

Notice the many possible *overtones* associated with $n \geq 2$. These decay more rapidly than the fundamental ($n = 1$), since the radial eigenfunctions possess $n - 1$ field reversals. For such overtones, the effective length scale to be used in the decay-time estimate is roughly the radial distance between the field reversals, or $\approx R/n$.

Figure 2.1 (top row) shows the first three fundamental ($n = 1$) modes of angular degrees $l = 1, 2, 3$, corresponding to dipolar, quadrupolar, and hexapolar magnetic fields, as well as a few higher overtones for $l = 1, 2$ (bottom row). The decay time estimate provided by Eq. (1.63) turns out to be too large by a factor $\pi^2 \approx 10$, for a sun with constant diffusivity. Still not so bad for a pure order-of-magnitude estimate!

2.1.3 Toroidal Field Decay

Computing the decay rate of a purely toroidal magnetic field follows the same basic logic. We now require $B = 0$ at $r = R$, and the decay rate ends up related to the zero of a spherical Bessel function—only of index l rather than $l - 1$ as was found for the decay of the poloidal field. Hence, a dipole ($l = 1$) toroidal magnetic field decays at precisely the same rate as a quadrupole ($l = 2$) poloidal magnetic field (still for constant diffusivity). Sneaking a peak in a handbook of special functions soon reveals that the decay rate of a $l = 1$ toroidal field follows from the transcendental equation:

$$\tan kR = kR \ . \tag{2.14}$$

The smallest non-zero solution of this equation gives,

$$\lambda_1 = \frac{\eta(4.493409\ldots)^2}{R^2} \ , \qquad l = 1 \text{ toroidal and } l = 2 \text{ poloidal} \ . \tag{2.15}$$

As with a purely poloidal field, higher radial overtones decay proportionally faster.

2.1.4 Results for a Magnetic Diffusivity Varying with Depth

We end this section by a brief examination of the diffusive decay of large-scale poloidal magnetic fields in the solar interior. The primary complication centers on the magnetic diffusivity, which is no longer constant throughout the domain, and turns out to be rather difficult to compute from first principles. To begin with, the depth variations of the temperature and density in a solar model causes the magnetic diffusivity to increase from about $10^{-2}\,\mathrm{m^2\,s^{-1}}$ in the central core to $\sim 1\,\mathrm{m^2\,s^{-1}}$ at the core–envelope interface. This already substantial variation is however dwarfed by the much larger increase in the net magnetic diffusivity expected in the turbulent environment of the convective envelope. We will look into this in some detail in Chap. 3, but for the time being let us simply take for granted that η is much larger in the envelope than in the core.

In order to examine the consequences of a strongly depth-dependent magnetic diffusivity for the diffusive eigenmodes, we consider a simplified situation whereby η assumes a constant value η_c in the core, a constant value η_e ($\gg \eta_c$) in the envelope, the transition occurring smoothly across a thin spherical layer coinciding with the core–envelope interface. Mathematically, such a variation can be expressed as

$$\eta(r) = \eta_c + \frac{\eta_e - \eta_c}{2}\left[1 + \mathrm{erf}\left(\frac{r - r_c}{w}\right)\right], \tag{2.16}$$

where $\mathrm{erf}\,(x)$ is the error function, r_c is the radius of the core–envelope interface, and w is the half-width of the transition layer.

We are still facing the 1D eigenvalue problem presented by Eq. (2.10)! Expressing time in units of the diffusion time R^2/η_e based on the envelope diffusivity, we seek numerical solutions, subjected to the boundary conditions $f_\lambda(0) = 0$ and smooth matching to a potential field solution in $r/R > 1$, with the diffusivity ratio $\Delta\eta = \eta_c/\eta_e$ as a parameter of the model. Since we can make a reasonable guess at the first few eigenvalues on the basis of the diffusion time and adopted values of l and η_c ($\sim \pi^2 nl\Delta\eta$, for l and n not too large), a (relatively) simple technique such as inverse iteration is well-suited to secure both eigenvalues and eigenfunctions for the problem.

Figure 2.2 shows the radial eigenfunctions for the slowest decaying poloidal eigenmodes ($l = 1, n = 1$), with $r_c/R = 0.7$, $w/R = 0.05$ in Eq. (2.16) and diffusivity contrasts $\Delta\eta = 1$ (constant diffusivity), 10^{-1} and 10^{-3}. The corresponding eigenvalues, in units of R^2/η_e, are $\lambda = 9.87$, 2.14 and 0.028. Clearly, the (global) decay time is regulated by the region of *smallest* diffusivity, since λ scales approximately as $(\Delta\eta)^{-1}$. Notice also how the eigenmodes are increasingly concentrated in the core region ($r/R \lesssim 0.7$) as $\Delta\eta$ decreases, i.e., they are "expelled" from the convective envelope.

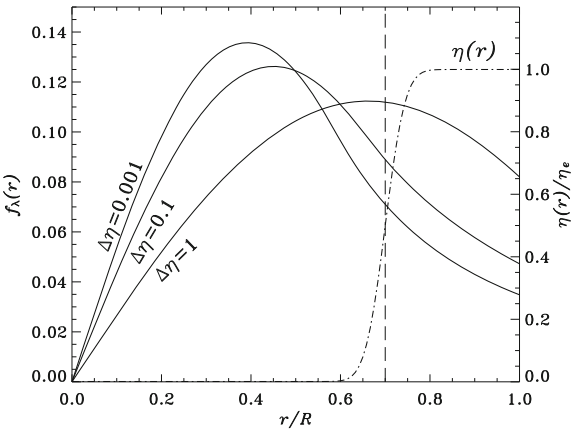

Fig. 2.2 Radial eigenfunctions for the slowest decaying ($\ell = 1$) poloidal eigenmodes ($l = 1$, $n = 1$) in a sphere embedded in a vacuum. The diffusivity is computed using Eq. (2.16) with $r_c/R = 0.7$, $w/R = 0.05$, and for three values of the core-to-envelope diffusivity ratio ($\Delta\eta$). The eigenvalues, in units of η_e/R^2, are $\lambda = 9.87$, 2.14 and 0.028 for $\Delta\eta = 1$, 0.1, and 10^{-3}, respectively. The diffusivity profile for $\Delta\eta = 10^{-3}$ is also plotted (*dash-dotted line*). The *vertical dashed line* indicates the location of the core–envelope interface.

2.1.5 Fossil Stellar Magnetic Fields

The marked decrease of the diffusive decay time with increasing angular and radial degrees of the eigenmodes is a noteworthy result. It means that left to decay long enough, any arbitrarily complex magnetic field in the sun or stars will eventually end up looking dipolar. Conversely, a fluid flow acting as a dynamo in a sphere and trying to "beat" Ohmic dissipation can be expected to preferentially produce a magnetic field approximating diffusive eigenmodes of low angular and radial degrees (or some combination thereof), since these are the least sensitive to Ohmic dissipation.

There exists classes of early-type main-sequence stars, i.e., stars hotter and more luminous than the sun and without deep convective envelope, that are believed to contain strong, large-scale fossil magnetic fields left over from their contraction toward the main-sequence. The chemically peculiar Ap/Bp stars are the best studied class of such objects. Reconstruction of their surface magnetic field distribution suggests almost invariably that the fields are dominated by a large-scale dipole-like component, as one would have expected from the preceding discussion if the observed magnetic fields have been diffusively decaying for tens or hundreds of millions of years. It is indeed quite striking that the highest strengths of large-scale magnetic fields in main-sequence stars (a few T in Ap stars), in white dwarfs ($\sim 10^5$ T) and in the most strongly magnetized neutron stars ($\sim 10^{11}$ T) all amount to similar total surface magnetic fluxes, $\sim 10^{19}$ Wb, lending support to the idea that these high field strengths can be understood from simple flux-freezing arguments (Sect. 1.10),

with field amplification resulting directly from magnetic flux conservation as the star shrinks to form a compact object. We will revisit the origin of A-star magnetic fields in Chap. 5.

2.2 Magnetic Field Amplification by Stretching and Shearing

Having thus investigated in some details the resistive decay of magnetic field, we turn to the other physical mechanism embodied in Eq. (1.59): growth of the magnetic field in response to the inductive action of a flow $\boldsymbol{u}$. We first take a quick look at field amplification in a few idealized model flows, and then move on to a specific example involving a "real" astrophysical flow.

2.2.1 Hydrodynamical Stretching and Field Amplification

Let's revert for a moment to the ideal MHD case ($\eta = 0$). The induction equation can then be expressed as

$$\left(\frac{\partial}{\partial t} + \boldsymbol{u}\cdot\nabla\right)\boldsymbol{B} = \boldsymbol{B}\cdot\nabla\boldsymbol{u}\ , \tag{2.17}$$

where it was further assumed that the flow is incompressible ($\nabla\cdot\boldsymbol{u} = 0$). The LHS of Eq. (2.17) is the Lagrangian derivative of $\boldsymbol{B}$, expressing the time rate of change of $\boldsymbol{B}$ in a fluid element moving with the flow. The RHS expresses the fact that this rate of change is proportional to the local *shear* in the flow field. Shearing has the effect of *stretching* magnetic fieldlines, which is what leads to magnetic field amplification.

As a simple example, consider on Fig. 2.3 a cylindrical fluid element of length L_1, threaded by a constant magnetic field of strength B_1 oriented parallel to the axis of the cylinder. In MHD, such a magnetic field could be sustained by an azimuthal current concentrated in a thin sheet coinciding with the outer boundary of the cylinder, giving a solenoid-like current+field system. Assume now that this magnetic "flux tube" is embedded in a perfectly conducting incompressible fluid and subjected to a stretching motion ($\partial u_z/\partial z > 0$) along its central axis such that its length increases to L_2. Mass conservation demands that

$$\frac{R_2}{R_1} = \sqrt{\frac{L_1}{L_2}}\ . \tag{2.18}$$

Conservation of the magnetic flux ($= \pi R^2 B$), in turn, leads to

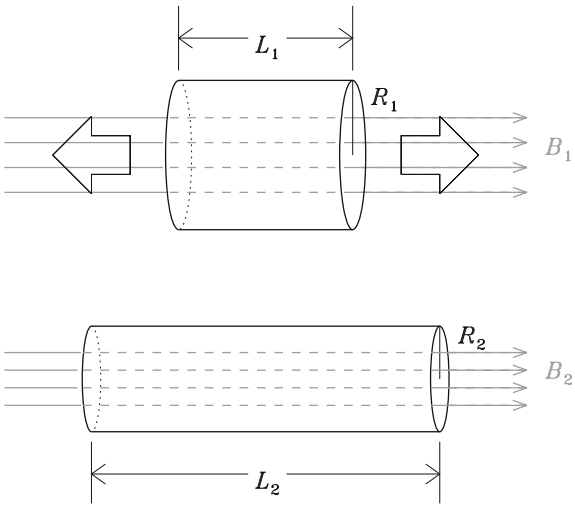

Fig. 2.3 Stretching of a magnetized cylindrical fluid element by a diverging flow. The magnetic field (*fieldlines in gray*) is horizontal within the tube, has a strength B_1 originally, and B_2 after stretching. In the flux-freezing limit, mass conservation within the tube requires its radius to decrease, which in turn leads to field amplification (see text).

$$\frac{B_2}{B_1} = \frac{L_2}{L_1} \,, \tag{2.19}$$

i.e., the field strength is amplified in direct proportion to the level of stretching.

This almost trivial result is in fact at the very heart of *any* magnetic field amplification in the magnetohydrodynamical context, and illustrates two crucial aspects of the mechanism: first, this works only if the fieldlines are frozen into the fluid, i.e., in the high-$\mathrm{R_m}$ regime. Second, mass conservation plays an essential role here; the stretching motion along the tube axis *must* be accompanied by a compressing fluid motion perpendicular to the axis if mass conservation is to be satisfied. It is this latter compressive motion, occurring perpendicular to the magnetic fieldlines forming the flux tube, that is ultimately responsible for field amplification; the horizontal fluid motion occurs parallel to the magnetic fieldline, and so cannot in itself have any inductive effect as per Eq. (1.59). This becomes evident upon considering the transfer of energy in this magnetized fluid system. With the electrical current sustaining the magnetic field concentrated in a thin cylindrical sheet bounding the tube, the field is force-free everywhere except at the surface of the tube, where the Lorentz force points radially outwards. It is the work done by the flow against this force which transfers energy from the flow to the magnetic field, and ultimately ends up in magnetic energy (viz. Eq. (1.87)).

The challenge, of course, is to realize this idealized scenario in practice, i.e., to find a flow which achieves the effect illustrated on Fig. 2.3. This, it turns out, is much simpler than one might expect! Working in cylindrical coordinates (s, ϕ, z), consider the following incompressible flow:

$$u_s(s) = \frac{\alpha s}{2} \,, \qquad u_\phi = 0 \,, \qquad u_z(z) = -\alpha z \,, \tag{2.20}$$

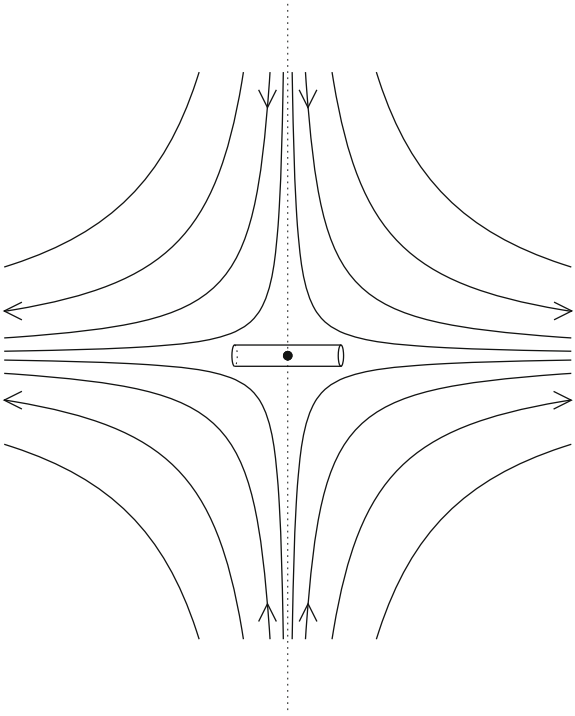

Fig. 2.4 Streamlines of the stagnation point flow defined by Eq. (2.20), plotted in a constant-ϕ plane. The flow is rotationally invariant about the symmetry (z) axis, indicated by the *dotted line*, and the stagnation point (*solid dot*) is located at the origin of the cylindrical coordinate system. A thin magnetic flux tube located in the $z = 0$ plane and crossing the origin, as shown, will be subjected to the stretching motion illustrated in cartoon form on Fig. 2.3.

with $\alpha > 0$. This describes a flow converging towards the $z = 0$ plane along the z-axis, and diverging radially away from the origin within the $z = 0$ plane. Clearly, $\boldsymbol{u} = 0$ at the origin $(0, \phi, 0)$ of the cylindrical coordinate system. This is called a *stagnation point*, and its presence is vital to the inductive amplification of the magnetic field. Now place a thin, straight magnetic flux tube in the $z = 0$ plane, and enclosing the stagnation point, as shown on Fig. 2.4. You can easily verify that you will get exactly the type of stretching effect illustrated in cartoon form on Fig. 2.3.

2.2.2 The Vainshtein & Zeldovich Flux Rope Dynamo

So, the linear stretching of a flux tube amplifies the magnetic field, but the magnetic flux remains constant by the very nature of the amplification mechanism. Nonetheless, this idea actually forms the basis of a dynamo that can increase both the magnetic field strength and flux. S. Vainshtein and Ya. B. Zeldovich have proposed one of the first and justly celebrated "cartoon" model for this idea, as illustrated on Fig. 2.5. The steps are the following:

1. A circular rope of magnetic field is stretched to twice its length ($a \rightarrow b$). As we just learned, this doubles the magnetic field strength while conserving the flux;

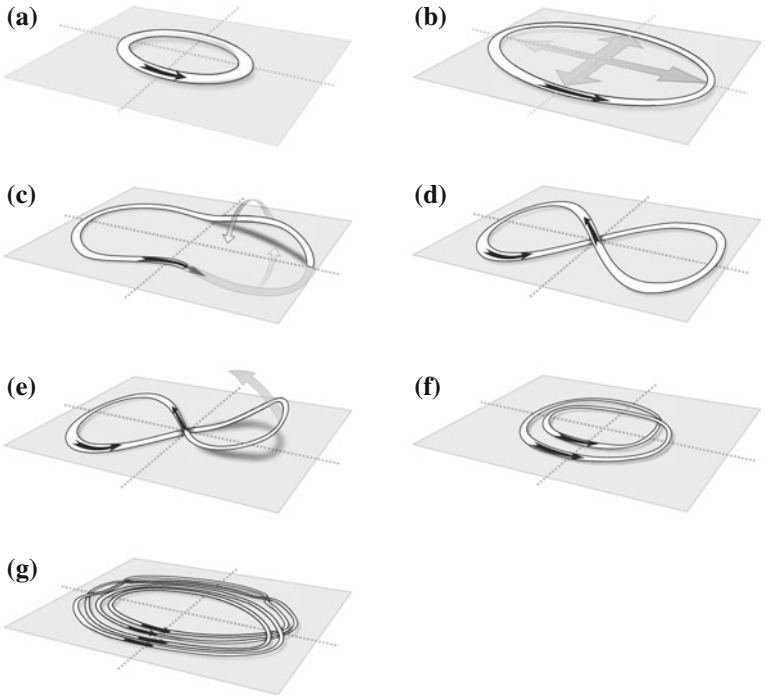

Fig. 2.5 Cartoon of the Stretch–Twist–Fold flux rope dynamo of Vainshtein & Zeldovich. A circular flux rope is (**a** → **b**) stretched, (**c** → **d**) twisted, and (**e** → **f**) folded. Diagram **g** shows the resulting structure after another such sequence acting on (**f**). Diagram produced by D. Passos.

2. The rope is twisted by half a turn ($c \rightarrow d$);
3. One half of the rope is folded over the other half in such a way as to align the magnetic field of each half ($e \rightarrow f$); this now doubles the magnetic flux through any plane crossed by the stacked loops.

This is quite remarkable; the so-called *stretch–twist–fold* sequence (hereafter STF) illustrated on Fig. 2.5 first doubles the field strength while conserving the magnetic flux of the original rope, because the tube's cross-section ($\propto R^2$) varies as the inverse of its length (as per Eq. 2.18), then folding doubles the magnetic flux without reducing the field strength since the loop's cross-section remains unaffected. If the sequence is repeated n times, the magnetic field strength (and flux) is then amplified by a factor

$$\frac{B^n}{B_0} \propto 2^n = \exp(n \ln 2) \ . \tag{2.21}$$

With n playing the role of a (discrete) time-like variable, Eq. (2.21) indicates an exponential growth of the magnetic field, with a growth rate $\sigma = \ln 2$. Rejoice! This is our first dynamo!

A concept central to the STF dynamo—and other dynamos to be encountered later—is that of *constructive folding*. Note how essential the twisting step is to the STF dynamo: without it (or with an even number of twists), the magnetic field in each half of the folded rope would end up pointing in opposite direction, and would then add up to zero net flux, a case of *destructive folding*. We'll have more to say on the STF dynamo later on; for now we turn to amplification by fluid motions that shear rather than stretch.

2.2.3 Hydrodynamical Shearing and Field Amplification

Magnetic field amplification by stretching, as illustrated on Fig. 2.3, evidently requires (1) a stagnation point in the flow, and (2) a rather specific positioning and orientation of the flux tube with respect to this stagnation point. We will encounter later more realistic flows that do achieve field amplification through stretching in the vicinity of stagnation points, but there is a different type of fluid motion that can produce a more robust form of magnetic field amplification: *shearing*.

The idea is illustrated in cartoon form on Fig. 2.6. We start with a magnetic flux tube, as before, but this time the flow is everywhere perpendicular to the axis of the tube, and its magnitude varies with height along the length of the tube, e.g., $\boldsymbol{u} = u_x(z)\hat{\boldsymbol{e}}_x$, so that $\partial u_x/\partial z \neq 0$; this is called a *planar sheared flow*. In the ideal MHD limit, every small section of the tube is displaced sideways at a rate equal to the flow speed. After a while, the tube will no longer be straight, and for the type of shearing motion illustrated on Fig. 2.6, its length will have increased. By the same logic as before, the field strength within the tube must have increased proportionally to the increase in length of the tube. Note also that here the action of the shear leaves the z-component of the magnetic field unaffected, but produces an x-component where there was initially none.

The beauty of this mechanism is that it does not require stagnation points, and will in general operate for any sheared flow. The latter turn out to be rather common in astrophysical objects, and we now turn to one particularly important example.

2.2.4 Toroidal Field Production by Differential Rotation

A situation of great (astro)physical interest is the induction of a toroidal magnetic field via the shearing of a pre-existing poloidal magnetic field threading a differentially rotating sphere of electrically conducting fluid. Working now in spherical polar coordinates (r, θ, ϕ) and assuming overall axisymmetry (i.e., the poloidal field and differential rotation share the same symmetry axis), the flow velocity can be written as:

$$\boldsymbol{u}(r, \theta) = \varpi\Omega(r, \theta)\hat{\boldsymbol{e}}_\phi \,, \tag{2.22}$$

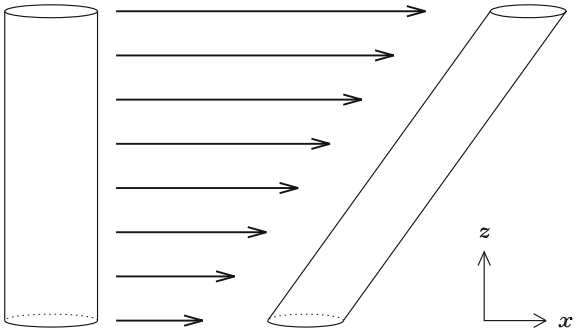

Fig. 2.6 Stretching of a flux tube by a shearing motion directed perpendicularly to the tube's axis. Unlike on Fig. 2.3, here the tube does not remain straight, but it's length is still increasing as a consequence of the tube's deformation; consequently, in the ideal MHD limit the magnetic field threading the tube will be amplified by a factor given by the ratio of its final to initial length, as per Eq. (2.19).

where again $\varpi = r \sin\theta$, and the angular velocity $\Omega(r, \theta)$ is assumed steady ($\partial/\partial t = 0$), corresponding to the kinematic regime introduced earlier. Once again, we take advantage of the poloidal/toroidal separation for axisymmetric magnetic fields (introduced in Sect. 2.1). For the (divergenceless) azimuthal flow $\boldsymbol{u}$ given by the above expression, $\nabla \times (\boldsymbol{u} \times \boldsymbol{B}) = (\boldsymbol{B} \cdot \nabla)\boldsymbol{u} - (\boldsymbol{u} \cdot \nabla)\boldsymbol{B}$, which for an axisymmetric magnetic field only has a non-zero contribution in the ϕ-direction since $\boldsymbol{u}$ itself is azimuthally-directed.[2]

If moreover one neglects magnetic dissipation, the induction equation now separates into:

$$\frac{\partial A}{\partial t} = 0 \,, \tag{2.23}$$

$$\frac{\partial B}{\partial t} = \varpi[\nabla \times (A\hat{\boldsymbol{e}}_\phi)] \cdot \nabla\Omega \,. \tag{2.24}$$

Equation (2.23) states that the poloidal component remains constant in time, so that Eq. (2.24) integrates immediately to

$$B(r, \theta, t) = B(r, \theta, 0) + \Big(\varpi[\nabla \times (A\hat{\boldsymbol{e}}_\phi)] \cdot \nabla\Omega\Big)t \,. \tag{2.25}$$

Anywhere in the domain, the toroidal component of the magnetic field grows linearly in time, at a rate proportional to the net local shear and local poloidal field strength. A toroidal magnetic component is being generated by shearing the

[2] In trying to demonstrate this, keep in mind that $\boldsymbol{B} \cdot \nabla$ and $\boldsymbol{u} \cdot \nabla$ are differential operators acting on *vector* quantities; it may come as a surprise to realize that $(\boldsymbol{B} \cdot \nabla)\boldsymbol{u}$ has non-vanishing r- and θ-components, even though $\boldsymbol{u}$ is azimuthally-directed! See Appendix A for the component form of these operators in spherical polar coordinates.

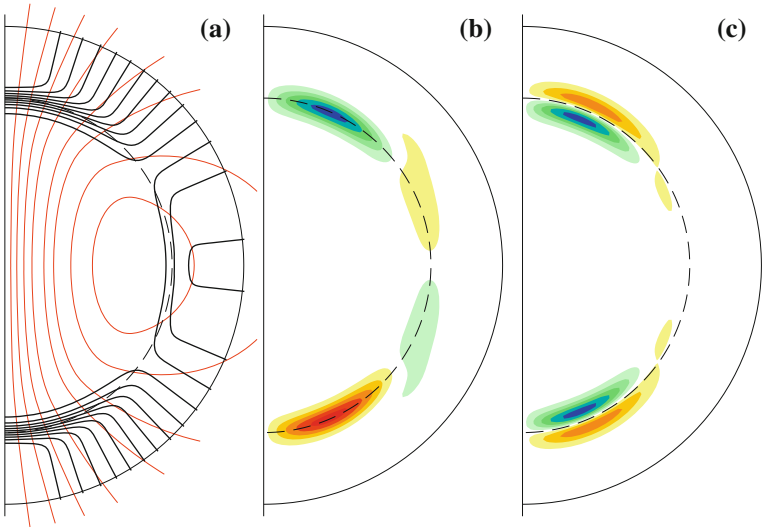

Fig. 2.7 Shearing of a poloidal field into a toroidal component by a solar-like differential rotation profile. Part **a** shows isocontours of the rotation rate $\Omega(r,\theta)/2\pi$ (*solid lines*, contour spacing 10 nHz). The *red lines* are fieldlines for the $n = 1$ dipolar diffusive eigenmode with core-to-envelope diffusivity contrast $\Delta\eta = 10^{-2}$. The *dashed line* is the core–envelope interface at $r/R = 0.7$. Part **b** shows isocontours of the toroidal field, with *yellow-red* (*green-blue*) corresponding to positive (negative) B, after 10 yr of shearing. The maximum toroidal field strength is about 0.2 T, and contour spacing is 0.02 T. Part **c** shows logarithmically spaced isocontours of the ϕ-component of the Lorentz force associated with the poloidal/toroidal fields of panels (**a**) and (**b**).

initially purely poloidal fieldlines in the ϕ-direction, and the magnitude of the poloidal magnetic component remains unaffected, as per Eq. (2.23). Note also that for such an axisymmetric configuration, the only possible steady-state ($\partial/\partial t = 0$) solutions must have

$$[\nabla \times (A\hat{\boldsymbol{e}}_\phi)] \cdot \nabla\Omega = 0 \,, \tag{2.26}$$

i.e., the angular velocity must be constant on any given poloidal flux surface. This result is known as *Ferraro's theorem*.

Evidently, computing B via Eq. (2.25) requires a knowledge of the solar internal (differential) rotation profile $\Omega(r,\theta)$. Consider the following parametrization:

$$\Omega(r,\theta) = \Omega_C + \frac{\Omega_S(\theta) - \Omega_C}{2}\left[1 + \mathrm{erf}\left(\frac{r - r_C}{w}\right)\right] \,, \tag{2.27}$$

where

$$\Omega_S(\theta) = \Omega_{Eq}(1 - a_2\cos^2\theta - a_4\cos^4\theta) \tag{2.28}$$

is the surface latitudinal differential rotation. We will make repeated use of this parametrization in this and following chapters, so let's look into it in some detail.

Figure 2.7a shows isocontours of angular velocity (in black) generated by the above parameterization with parameter values $\Omega_C/2\pi = 432.8\,\text{nHz}$, $\Omega_{Eq}/2\pi = 460.7\,\text{nHz}$, $a_2 = 0.1264$, $a_4 = 0.1591$, $r_c = 0.713R$, and $w = 0.05R$, as obtained by a best-fit to helioseismic frequency splittings. This properly reproduces the primary features of full helioseismic inversions, namely:

1. A convective envelope ($r \gtrsim r_c$) where the shear is purely latitudinal, with the equatorial region rotating faster than the poles;
2. A core ($r \lesssim r_c$) that rotates rigidly, at a rate equal to that of the surface mid-latitudes;
3. A smooth matching of the core and envelope rotation profiles occurring across a thin spherical layer coinciding with the core–envelope interface ($r = r_c$), known as the *tachocline*.

It should be emphasized already at this juncture that such a solar-like differential rotation profile is quite complex, in that it is characterized by *three* partially overlapping shear regions: a strong positive radial shear (i.e., $\partial\Omega/\partial r > 0$) in the equatorial regions of the tachocline, an even stronger negative radial shear ($\partial\Omega/\partial r < 0$) in its polar regions, and a significant positive latitudinal shear ($\partial\Omega/\partial\theta > 0$) throughout the convective envelope and extending partway into the tachocline. For a tachocline of half-thickness $w/R = 0.05$, the mid-latitude latitudinal shear at $r/R = 0.7$ is comparable in magnitude to the equatorial radial shear; as we will see in the next chapter, its potential contribution to dynamo action should not be casually dismissed.

Figure 2.7b shows the distribution of toroidal magnetic field resulting from the shearing of the slowest decaying, $n = 1$ dipole-like diffusive eigenmode of Sect. 2.1 of strength $10^{-4}\,\text{T}$ at $r/R = 0.7$, using the diffusivity profile given by Eq. (2.16) with diffusivity contrast $\Delta\eta = 10^{-2}$ (part a, red lines). This is nothing more than Eq. (2.25) evaluated for $t = 10\,\text{yr}$, with $B(r, \theta, 0) = 0$. Not surprisingly, the toroidal field is concentrated in the regions of large radial shear, at the core–envelope interface (dashed line). Note how the toroidal field distribution is *antisymmetric* about the equatorial plane, precisely what one would expect from the inductive action of a shear flow that is equatorially symmetric on a poloidal magnetic field that is itself antisymmetric about the equator.

Knowing the distributions of toroidal and poloidal fields on Fig. 2.7 allows us to flirt a bit with dynamics, by computing the Lorentz force. For the axisymmetric magnetic field considered here, the ϕ-component of Eq. (1.75) reduces to:

$$[\boldsymbol{F}]_\phi = \frac{1}{\mu_0 \varpi} \boldsymbol{B}_p \cdot \nabla(\varpi B) \,, \tag{2.29}$$

with $\boldsymbol{B}_p = \nabla \times (A\hat{\boldsymbol{e}}_\phi)$ the poloidal field. The resulting spatial distribution of $[\boldsymbol{F}]_\phi$ is plotted on Fig. 2.7c. Examine this carefully to convince yourself that the Lorentz force is such as to *oppose* the driving shear. This is an important and totally general property of interacting flows and magnetic fields: the Lorentz force tends to resist the hydrodynamical shearing responsible here for field induction. The ultimate fate of the system depends on whether the Lorentz force becomes dynamically significant

before the growth of the toroidal field is mitigated by resistive dissipation: this is likely the case in solar/stellar interiors.

Clearly, the growing magnetic energy of the toroidal field is supplied by the kinetic energy of the rotational shearing motion (this is hidden in the second term on the RHS of Eq. (1.87)). In the solar case, this is an attractive field amplification mechanism, because the available supply of rotational kinetic energy is immense.[3] But don't make the mistake of thinking that this is a dynamo! In obtaining Eq. (2.25) we have completely neglected magnetic dissipation, and remember, the dynamos we are seeking are flows that can amplify and sustain a magnetic field *against* Ohmic dissipation. In fact, neither flux tube stretching (Fig. 2.3) or shearing (Fig. 2.6) is a dynamo either, for the same reason.[4] Nonetheless, shearing of a poloidal field by differential rotation will turn out to be a central component of *all* solar/stellar dynamo models constructed in later chapters. It is also believed to be an important ingredient of magnetic amplification in stellar accretion disks, and even in galactic disks.

2.3 Magnetic Field Evolution in a Cellular Flow

Having examined separately the resistive decay and hydrodynamical induction of magnetic field, we now turn to a situation where both processes operate simultaneously.

2.3.1 A Cellular Flow Solution

Working now in Cartesian geometry, we consider the action of a steady, incompressible ($\nabla \cdot \boldsymbol{u} = 0$) two-dimensional flow

$$\boldsymbol{u}(x, y) = u_x(x, y)\hat{\boldsymbol{e}}_x + u_y(x, y)\hat{\boldsymbol{e}}_y \tag{2.30}$$

on a two-dimensional magnetic field

$$\boldsymbol{B}(x, y, t) = B_x(x, y, t)\hat{\boldsymbol{e}}_x + B_y(x, y, t)\hat{\boldsymbol{e}}_y \ . \tag{2.31}$$

Note that neither the flow nor the magnetic field have a z-component, and that their x and y-components are both independent of the z-coordinate. The flow is said to be *planar* because $u_z = 0$, and has an ignorable coordinate (i.e., translational

[3] This may no longer be the case, however, if dynamo action takes place in a thin layer below the base of the convective envelope; see the paper by see the paper by Steiner & Ferris-Mas (2005) in the bibliography of the next chapter, for more on this aspect of the problem.

[4] The STF dynamo (Fig. 2.5) is the lone exception here, in that it remains a dynamo even when magnetic dissipation is brought into the picture; the reasons why are subtle and will be clarified later on.

symmetry) since $\partial/\partial z \equiv 0$ for all field and flow components. Such a magnetic field can be represented by the vector potential

$$\boldsymbol{A} = A(x, y, t)\hat{\boldsymbol{e}}_z \,, \tag{2.32}$$

where, as usual, $\boldsymbol{B} = \nabla \times \boldsymbol{A}$. Under this representation, lines of constant A in the $[x, y]$ plane coincide with magnetic fieldlines. The only non-trivial component of the induction equation (1.97) is its z-components, which takes the form

$$\frac{\partial A}{\partial t} + \boldsymbol{u} \cdot \nabla A = \eta \nabla^2 A \,. \tag{2.33}$$

This is a linear advection-diffusion equation, describing the transport of a passive scalar quantity A by a flow $\boldsymbol{u}$, and subject to diffusion, the magnitude of which being measured by η. In view of the symmetry and planar nature of the flow, it is convenient to write the 2D flow field in terms of a stream function $\Psi(x, y)$:

$$\boldsymbol{u}(x, y) = u_0 \left(\frac{\partial \Psi}{\partial y} \hat{\boldsymbol{e}}_x - \frac{\partial \Psi}{\partial x} \hat{\boldsymbol{e}}_y \right) \,. \tag{2.34}$$

It is easily verified that any flow so defined will identically satisfy the condition $\nabla \cdot \boldsymbol{u} = 0$. As with Eq. (2.32), a given numerical value of Ψ uniquely labels one streamline of the flow. Consider now the stream function

$$\Psi(x, y) = \frac{L}{4\pi} \left(1 - \cos\left(\frac{2\pi x}{L} \right) \right) \left(1 - \cos\left(\frac{2\pi y}{L} \right) \right), \quad x, y \in [0, L] \,. \tag{2.35}$$

This describes a counterclockwise cellular flow centered on $(x, y) = (L/2, L/2)$ as shown on Fig. 2.8. The maximal velocity amplitude $\max \|\boldsymbol{u}\| = u_0$ is found along the streamline $\Psi = u_0 L/(2\pi)$, plotted as a thicker line on Fig. 2.8. This streamline is well approximated by a circle of radius $L/4$, and its streamwise circulation period turns out to be $1.065\,\pi L/2u_0$, quite close to what one would expect in the case of a perfectly circular streamline. In what follows, this timescale is denoted τ_c and referred to as the *turnover time* of the flow. Note that both the normal and tangential components of the flow vanish on the boundaries $x = 0, L$ and $y = 0, L$. This implies that the domain boundary is itself a streamline ($\Psi = 0$, in fact), and that every streamline interior to the boundary closes upon itself within the spatial domain.

We now investigate the inductive action of this flow by solving a nondimensional version of Eq. (2.33), by expressing all lengths in units of L, and time in units of L/u_0, so that

$$\frac{\partial A}{\partial t} = -\frac{\partial \Psi}{\partial y}\frac{\partial A}{\partial x} + \frac{\partial \Psi}{\partial x}\frac{\partial A}{\partial y} + \frac{1}{\mathrm{R_m}} \left(\frac{\partial^2 A}{\partial x^2} + \frac{\partial^2 A}{\partial y^2} \right) \,, \quad x, y \in [0, L] \,, \tag{2.36}$$

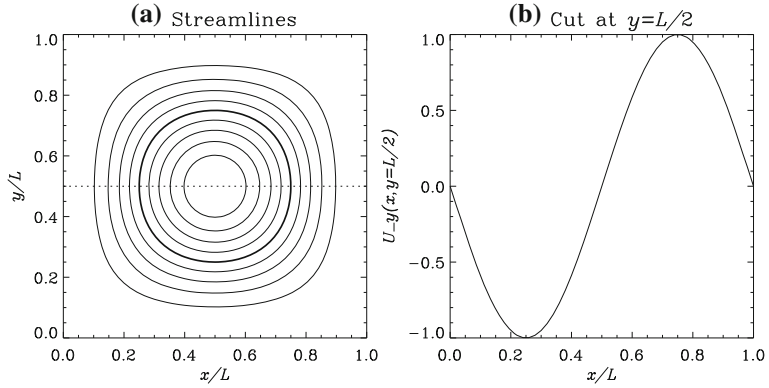

Fig. 2.8 Counterclockwise cellular flow generated by the streamfunction given by Eq. (2.35). Part **a** shows streamlines of the flow, with the thicker streamline corresponding to $\Psi = u_0 L/(2\pi)$, on which the flow attains its maximum speed u_0. Part **b** shows the profile of $u_y(x)$ along a horizontal cut at $y = 1/2$. A "typical" length scale for the flow is then $\sim L$.

where $\mathrm{R_m} = u_0 L/\eta$ is the magnetic Reynolds number for this problem, and the corresponding diffusion time is then $\tau_\eta = \mathrm{R_m}$ in dimensionless units. Equation (2.36) is solved as an initial-boundary value problem in two spatial dimensions. All calculations described below start at $t = 0$ with an initially uniform, constant magnetic field $\boldsymbol{B} = B_0 \hat{\boldsymbol{e}}_x$, equivalent to:

$$A(x, y, 0) = B_0\, y\ . \tag{2.37}$$

We consider a situation where the magnetic field component normal to the boundaries is held fixed, which amounts to holding the vector potential fixed on the boundary.

Figure 2.9 shows the variation with time of the magnetic energy (Eq. 1.89), for four solutions having $\mathrm{R_m} = 10, 10^2, 10^3$ and 10^4. Figure 2.10 shows the evolving shape of the magnetic fieldlines in the $\mathrm{R_m} = 10^3$ solution at 9 successive epochs. The solid dots are "floaters", namely Lagrangian markers moving along with the flow. At $t = 0$ all floaters are equidistant and located on the fieldline initially coinciding with the coordinate line $y/L = 0.5$, that (evolving) fieldline being plotted in the same color as the floaters on all panels. Figure 2.10 covers two turnover times.[5]

At first, the magnetic energy increases quadratically in time. This is precisely what one would expect from the shearing action of the flow on the initial B_x-directed magnetic field, which leads to a growth of the B_y-component that is linear in time. However, for $t/\tau_\mathrm{c} \gtrsim 2$ the magnetic energy starts to decrease again and eventually $(t/\tau_\mathrm{c} \gg 1)$ levels off to a constant value. To understand the origin of this behavior we need to turn to Fig. 2.10 and examine the solutions in some detail.

[5] An animation of this solution, and related additional solutions, can be viewed on the course web-page http://obswww.unige.ch/SSAA/sf39/dynamos.

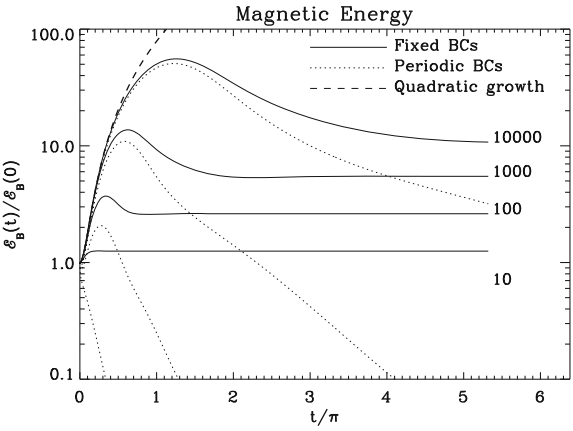

Fig. 2.9 Evolution of the magnetic energy for solutions with different values of R_m. The solutions have been computed over 10 turnover times, at which point they are getting reasonably close to steady-state, at least as far as magnetic energy is concerned. One turnover time corresponds to $t/\pi = 0.532$.

The counterclockwise shearing action of the flow is quite obvious on Fig. 2.10 in the early phases of the evolution, leading to a rather pretty spiral pattern as magnetic fieldlines get wrapped around one another. Note that the distortion of magnetic fieldlines by the flow implies a great deal of *stretching* in the streamwise direction, as well as *folding* in the cross-stream direction. The latter shows up as sharp bends in the fieldlines, while the former is most obvious upon noting that the distance between adjacent floaters increases monotonically in time. In other words, an imaginary flux tube enclosing this fieldline is experiencing the same type of stretching as on Fig. 2.6. It is no accident that the floaters end up in the regions of maximum field amplification on frames 2–5; they are initially positioned on the fieldline coinciding with the line $y = L/2$, everywhere perpendicular to the shearing flow (cf. Figs. 2.6 and 2.8), which pretty much ensures maximal inductive effect, as per Eq. (2.33).

That all floaters remain at first "attached" onto their original fieldline is what one would have expected from the fact that this is a relatively high-R_m solution, so that flux-freezing is effectively enforced. As the evolution proceeds, the magnetic field keeps building up in strength (as indicated by the color scale), but is increasingly confined to spiral "sheets" of decreasing thickness. Coincident with these sheets are strong electrical currents perpendicular to the plane of the page, the current density being given here by

$$J_z(x, y) = -\frac{1}{\mu_0}\nabla^2 A(x, y) \ . \tag{2.38}$$

This current density, integrated over the $[x, y]$ plane, exhibits a time-evolution resembling that of magnetic energy.

By the time we hit one turnover time (corresponding approximately to frame 5 on Fig. 2.10), it seems that we are making progress towards our goal of producing a dynamo; we have a flow field which, upon acting on a preexisting magnetic field, has intensified the strength of that field, at least in some localized regions of the spatial domain. However, beyond $t \sim \tau_c$ the sheets of magnetic fields are gradually

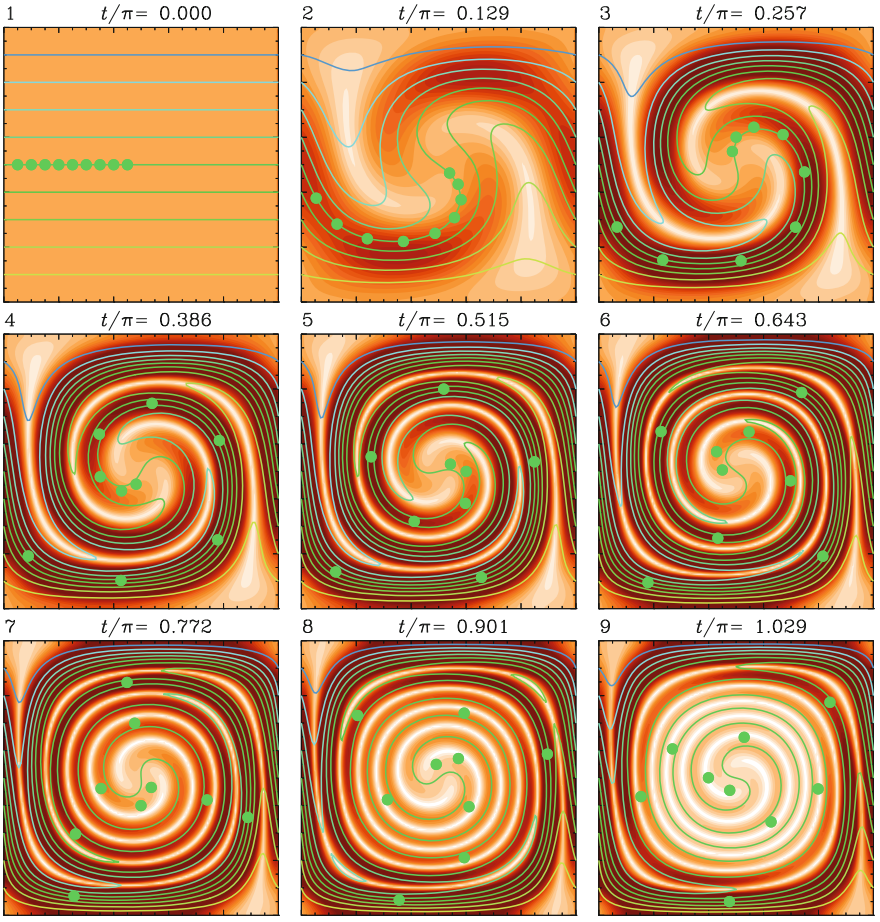

Fig. 2.10 Solution to Eq. (2.36) starting from an initially horizontal magnetic field. The panels show the shape of the magnetic fieldlines at successive times. The color scale encodes the absolute strength of the magnetic field, i.e., $\sqrt{B_x^2 + B_y^2}$. The x- and y-axes are horizontal and vertical, respectively, and span the range $x, y \in [0, L]$. Time t is in units of L/u_0. The *solid dots* are "floaters", i.e., Lagrangian marker passively advected by the flow. The magnetic Reynolds number is $\mathrm{R_m} = 10^3$.

disappearing, first near the center of the flow cell (frames 5–7), and later everywhere except close to the domain boundaries (frames 7–9). Notice also how, from frame 5 onward, the floaters are seen to "slip" off their original fieldlines. This means that flux-freezing no longer holds; in other words, diffusion is taking place. Yet, we evidently still have $t \ll \tau_\eta$ ($\equiv \mathrm{R_m} = 10^3$ here), which indicates that diffusion should not yet have had enough time to significantly affect the solution. What is going on here?

2.3.2 *Flux Expulsion*

The solution to this apparent dilemma lies with the realization that we have defined R_m in terms of the global length scale L characterizing the flow. This was a perfectly sensible thing to do on the basis of the flow configuration and initial condition on the magnetic field. However, as the evolution proceeds beyond $\sim\tau_c$ the decreasing thickness of the magnetic field sheets means that the global length scale L is no longer an adequate measure of the "typical" length scale of the magnetic field, which is what is needed to estimate the diffusion time τ_η (see Eq. (1.63)).

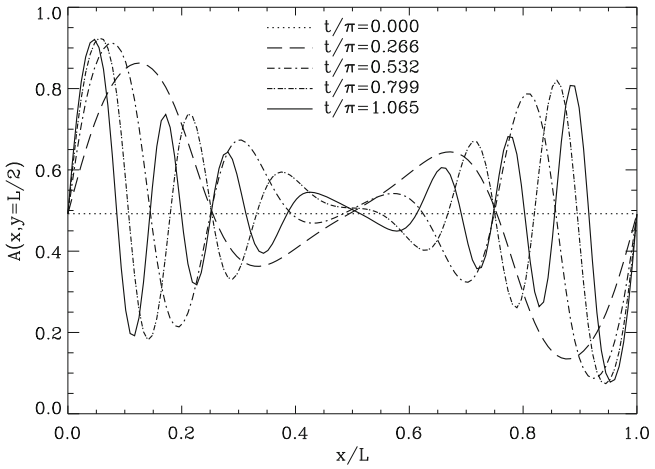

Fig. 2.11 Cuts of a $R_m = 10^4$ solution along the coordinate line $y = 0.5$, at successive times. Note how the "typical" length scale ℓ for the solution decreases with time, from $\ell/L \sim 0.25$ at $t/\pi = 0.266$, down to $\ell/L \sim 0.05$ after two turnover times ($t/\pi = 1.065$).

Figure 2.11 shows a series of cuts of the vector potential A in a $R_m = 10^4$ solution, plotted along the coordinate line $y = L/2$, at equally spaced successive time intervals covering two turnover times. Clearly the inexorable winding of the fieldline leads to a general decrease of the length scale characterizing the evolving solution. In fact, each turnover time adds two new "layers" of alternating magnetic polarity to the spiraling sheet configuration, so that the average length scale ℓ decreases as t^{-1}:

$$\frac{\ell(t)}{L} \propto \frac{L}{u_0 t} \ , \tag{2.39}$$

which implies in turn that the *local* dissipation time, $\propto \ell^2/\eta$, is decreasing as t^{-2}. On the other hand, examination of Fig. 2.10 soon reveals that the (decreasing) length scale characterizes the thickness of elongated magnetic structures that are themselves more or less *aligned* with the streamlines, so that the turnover time τ_c remains the proper timescale measuring field induction. With τ_c fixed and τ_η inexorably

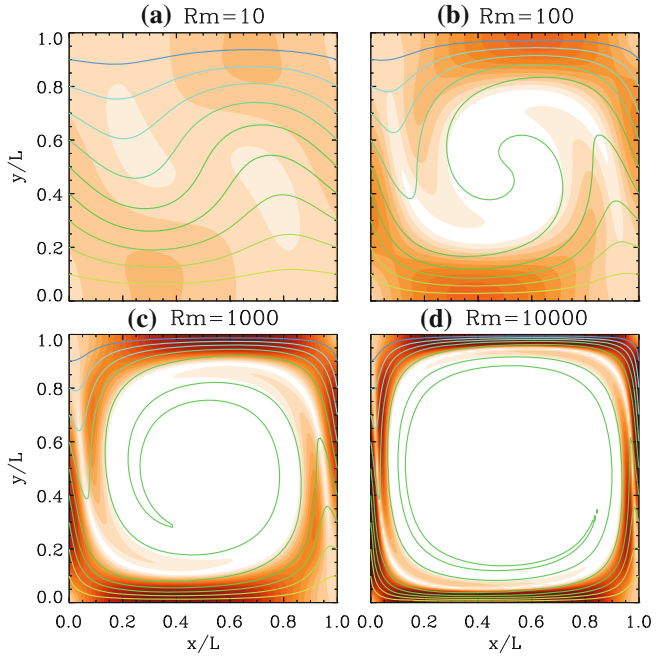

Fig. 2.12 Steady-state solutions to the cellular flow problem, for increasing values of the magnetic Reynolds number $\mathrm{R_m}$. The $\mathrm{R_m} = 10^4$ solution is at the resolution limit of the $N_x \times N_y = 128 \times 128$ mesh used to obtain these solutions, as evidenced on part (**d**) by the presence of small scale irregularities where magnetic fieldlines are sharply bent. The color scale encodes the local magnitude of the magnetic field. Note how, in the higher $\mathrm{R_m}$ solutions, magnetic flux is expelled from the center of the flow cell. With $\mathcal{E}_B(0)$ denoting the energy of a purely horizontal field with same normal boundary flux distribution, the magnetic energy for these steady states is $\mathcal{E}_B/\mathcal{E}_B(0) = 1.37$, 2.80, 5.81 and 11.75, respectively, for panels (**a**) through (**d**).

decreasing, the solution is bound to reach a point where $\tau_\eta \simeq \tau_\mathrm{c}$, *no matter how small dissipation actually is*. To reach that stage just takes longer in the higher $\mathrm{R_m}$ solutions, since more winding of the fieldlines is needed. Larger magnetic energy can build up in the transient phase, but the growth of the magnetic field is *always* arrested even in the limit $\mathrm{R_m} \to 0$. Equating τ_c ($\sim L/u_0$) to the *local* dissipation time ℓ^2/η, one readily finds that the length scale ℓ at which both process become comparable can be expressed in terms of the *global* $\mathrm{R_m}$ as

$$\frac{\ell}{L} = (\mathrm{R_m})^{-1/2} , \qquad \mathrm{R_m} = \frac{u_0 L}{\eta} . \tag{2.40}$$

That such a balance between induction and dissipation materializes means that a steady-state can be attained. Figure 2.12 shows four such steady state solutions for increasing values of the (global) magnetic Reynolds number $\mathrm{R_m}$. The higher $\mathrm{R_m}$ solutions clearly show *flux expulsion* from the central regions of the domain. This

is a general feature of steady, high-$\mathrm{R_m}$ magnetized flows with closed streamlines: magnetic flux is expelled from the regions of closed streamlines towards the edges of the flow cells, where it ends up concentrated in *boundary layers* which indeed have a thickness of order $\mathrm{R_m}^{-1/2}$, as suggested by Eq. (2.40), within which strong z-directed electrical currents flow—and dissipate! It is important to understand how and why this happens.

To first get an intuitive feel for how flux expulsion operates, go back to Fig. 2.10. As the flow wraps the fieldlines around one another, it does so in a manner that folds fieldlines of opposite polarity closer and closer to each other. When two such fieldlines are squeezed closer together than the dissipative length scale (Eq. (2.40)), resistive decay takes over and destroys the field faster than it is being stretched. This is an instance of *destructive folding*, and can only be avoided along the boundaries, where the normal component of the field is held fixed. For flux expulsion to operate, flux-freezing must be effectively enforced on the spatial scale of the flow. Otherwise the field is largely insensitive to the flow, and fieldlines are hardly deformed with respect to their initial configuration (as on panel (a) of Fig. 2.12).

Consider now the implication for the total magnetic flux across the domain; flux conservation requires that the normal flux $B_0 L$ imposed at the right and left boundaries must somehow cross the interior, otherwise Maxwell's equation, $\nabla \cdot \boldsymbol{B} = 0$, would not be satisfied; because of flux expulsion, it can only do so in the thin layers along the bottom and top boundaries. Since the thickness of these layers scales as $\mathrm{R_m}^{-1/2}$, it follows that the field strength therein scales as $\sqrt{\mathrm{R_m}}$, which in turn implies that the total magnetic energy in the domain also scales as $\sqrt{\mathrm{R_m}}$ in the $t \gg \tau_c$ limit.

2.3.3 Digression: The Electromagnetic Skin Depth

You may recall that a sinusoidally oscillating magnetic field imposed at the boundary of a conductor will penetrate the conductor with an amplitude decreasing exponentially away from the boundary and into the conductor, with a length scale called the *electromagnetic skin depth*:

$$\ell = \sqrt{\frac{2\eta}{\omega}} \,. \tag{2.41}$$

Now, go back to the cellular flow and imagine that you are an observer located in the center of the flow cell, looking at the domain boundaries while rotating with angular frequency $\propto u_0/L$; what you "see" in front of you is an "oscillating" magnetic field, in the sense that it flips sign with "angular frequency" u_0/L. The corresponding electromagnetic skin depth would then be

$$\frac{\ell}{L} = \sqrt{\frac{2\eta}{u_0 L}} \equiv \sqrt{\frac{2}{\mathrm{R_m}}} \,, \tag{2.42}$$

which basically corresponds to the thickness of the boundary layer where significant magnetic field is present in the steady-states shown on Fig. 2.12. How about that for a mind flip...

2.3.4 Timescales for Field Amplification and Decay

Back to our cellular flow. Flux expulsion or not, it is clear from Fig. 2.9 (solid lines) that some level of field amplification has occurred in the high $\mathrm{R_m}$ solutions, in the sense that $\mathcal{E}_B(t \to \infty) > \mathcal{E}_B(0)$. But is this a dynamo? The solutions of Fig. 2.12 have strong electric currents in the direction perpendicular to the plane of the paper, concentrated in boundary layers adjacent to the domain boundaries and subjected to resistive dissipation. Have we then reached our goal, namely to amplify and maintain a weak, preexisting magnetic field against Ohmic dissipation?

In a narrow sense yes, but a bit of reflection will show that the boundary conditions are playing a crucial role. The only reason that the magnetic energy does not asymptotically go to zero is that the normal field component is held fixed at the boundaries, which, in the steady-state, implies a non-zero Poynting flux into the domain across the left and right vertical boundaries. The magnetic field is not avoiding resistive decay because of field induction within the domain, but rather because external energy (and magnetic flux) is being pumped in through the boundaries. This is precisely what is embodied in the first term on the RHS of Eq. (1.87).

What if this were not the case? One way to work around the boundary problem is to replace the fixed flux boundary conditions by periodic boundary conditions on $\boldsymbol{B}$, which in terms of A becomes:

$$A(0, y) = A(L, y) \ , \qquad \frac{\partial A(x, 0)}{\partial y} = \frac{\partial A(x, L)}{\partial y} \ . \tag{2.43}$$

There is still a net flux across the horizontal boundaries at $t = 0$, but the boundary flux is now free to decay away along with the solution. Effectively, we now have an infinitely long row of contiguous flow cells, initially threaded by a horizontal magnetic field extending to $\pm\infty$. It is time to reveal that the hitherto unexplained dotted lines on Fig. 2.9 correspond in fact to solutions computed with such boundary conditions, for the same cellular flow and initial condition as before. The magnetic energy now decays to zero, confirming that the boundaries indeed played a crucial role in the sustenance of the magnetic field in our previous solutions. What is noteworthy is the rate at which it does so. In the absence of the flow and with freely decaying boundary flux, the initial field would diffuse away on a timescale $\tau_\eta \sim L^2/\eta$, which is equal to $\mathrm{R_m}$ in units of L/u_0. With the flow turned on, the decay proceeds at an accelerated rate because of the inexorable decrease of the typical length scale associated with the evolving solution, which we argued earlier varied as t^{-1}. What then is the typical timescale for this enhanced dissipation? The decay phase of the field (for $t \gg L/u_0$) is approximately described by

$$\frac{\partial A}{\partial t} = \eta \nabla^2 A \ . \tag{2.44}$$

An estimate for the dissipation timescale can be obtained once again via dimensional analysis, by replacing ∇^2 by $1/\ell^2$, as in Sect. 2.1 but with the important difference that ℓ is now a function of time:

$$\ell \to \ell(t) = \left(\frac{L}{t}\right)\left(\frac{L}{u_0}\right) \ , \tag{2.45}$$

in view of our previous discussion (cf. Fig. 2.11 and accompanying text). This leads to

$$\frac{\partial A}{\partial t} \simeq -\frac{\eta u_0^2 t^2}{L^4} A \ , \tag{2.46}$$

where the minus sign is introduced "by hand" in view of the fact that $\nabla^2 A < 0$ in the decay phase. Equation (2.46) integrates to

$$\frac{A(t)}{A_0} = \exp\left[-\frac{\eta u_0^2}{3L^4} t^3\right] = \exp\left[-\frac{1}{3\mathrm{R_m}}\left(\frac{u_0^3 t^3}{L^3}\right)\right] \ . \tag{2.47}$$

This last expression indicates that with t measured in units of L/u_0, the decay time scales as $\mathrm{R_m}^{1/3}$. This is indeed a remarkable situation: in the low magnetic diffusivity regime (i.e., high $\mathrm{R_m}$), the flow has in fact *accelerated* the decay of the magnetic field, even though large field intensification can occur in the early, transient phases of the evolution. This is not at all what a dynamo should be doing!

As it turns out, flux expulsion is even trickier than the foregoing discussion may have led you to believe! Flux expulsion destroys the mean magnetic field component directed *perpendicular* to the flow streamlines. It cannot do a thing to a mean component oriented *parallel* to streamlines. For completely general flow patterns and initial conditions, the dissipative phase with timescale $\propto \mathrm{R_m}^{1/3}$ actually characterizes the approach to a state where the advected trace quantity—here the vector potential A—becomes constant *along each streamline*, at a value $\bar{A}$ equal to the initial value of A averaged on each of those streamlines. For the cellular flow and initial conditions used above, this average turns out to be $\bar{A} = 0.5$ *for every streamline*, so that the $\mathrm{R_m}^{1/3}$ decay phase corresponds to the true decay of the magnetic field to zero amplitude. If $\bar{A}$ varies from one fieldline to the next, however, the $\mathrm{R_m}^{1/3}$ phase is followed by a third decay phase, which proceeds on a timescale $\sim \mathrm{R_m}$, since induction no longer operates ($\boldsymbol{u} \cdot \nabla A = 0$) and the typical length scale for A is once again L. At any rate, even with a more favorable initial condition we have further delayed field dissipation, but we still don't have a dynamo since dissipation will proceed inexorably, at best on the "long" timescale $\mathrm{R_m} \times (L/u_0)$.

2.3.5 Flux Expulsion in Spherical Geometry: Axisymmetrization

You may think that the flux expulsion problem considered in the preceding section has nothing to do with any astronomical objects you are likely to encounter in your astrophysical careers. Wrong!

Consider the evolution of a magnetic field pervading a sphere of electrically conducting fluid, with the solar-like differential rotation profile already encountered previously (Sect. 2.2.4 and Eqs. (2.27)–(2.28)), and with the field having initially the form of a dipole whose axis is inclined by an angle Θ with respect to the rotation axis ($\theta = 0$). Such a magnetic field can be expressed in terms of a vector potential having components:

$$A_r(r,\theta,\phi) = 0 \,, \tag{2.48}$$

$$A_\theta(r,\theta,\phi) = (R/r)^2 \sin\Theta(\sin\beta\cos\phi - \cos\beta\sin\phi) \,, \tag{2.49}$$

$$A_\phi(r,\theta,\phi) = (R/r)^2[\cos\Theta\sin\theta - \sin\Theta\cos\theta(\cos\beta\cos\phi + \sin\beta\sin\phi)] \,, \tag{2.50}$$

where β is the azimuthal angle locating the projection of the dipole axis on the equatorial plane.

Now, the vector potential for an inclined dipole can be written as the sum of two contributions, the first corresponding to an aligned dipole ($\Theta = 0$), the second to a perpendicular dipole ($\Theta = \pi/2$), their relative magnitude being equal to $\tan\Theta$. Since the governing equation is linear, the solution for an inclined dipole can be broken into two independent solutions for the aligned and perpendicular dipoles. The former is precisely what we investigated already in Sect. 2.2.4, where we concluded there that the shearing of an aligned dipole by an axisymmetric differential rotation would lead to the buildup of a toroidal component, whose magnitude would grow linearly in time at a rate set by the magnitude of the shear.

The solution for a perpendicular dipole is in many way similar to the cellular flow problem of Sect. 2.3. You can see how this may be the case by imagining looking from above onto the equatorial plane of the sphere; the fieldlines contained in that plane will have a curvature and will be contained within a circular boundary, yet topologically the situation is similar to the cellular flow studied in the preceding section: the (sheared) flow in the equatorial plane is made of closed, circular streamlines contained within that plane, so that we can expect flux expulsion to occur. The equivalent of the turnover time here is the differential rotation timescale, namely the time for a point located on the equator to perform a full 2π revolution with respect to the poles:

$$\tau_{\rm DR} = (\Omega_{\rm Equ} - \Omega_{\rm Pole})^{-1} \,. \tag{2.51}$$

For a freely decaying dipole, the perpendicular component of the initial dipole will then be subjected to flux expulsion, and dissipated away, at a rate far exceeding purely diffusive decay in the high $\mathrm{R_m}$ limit, as argued earlier.

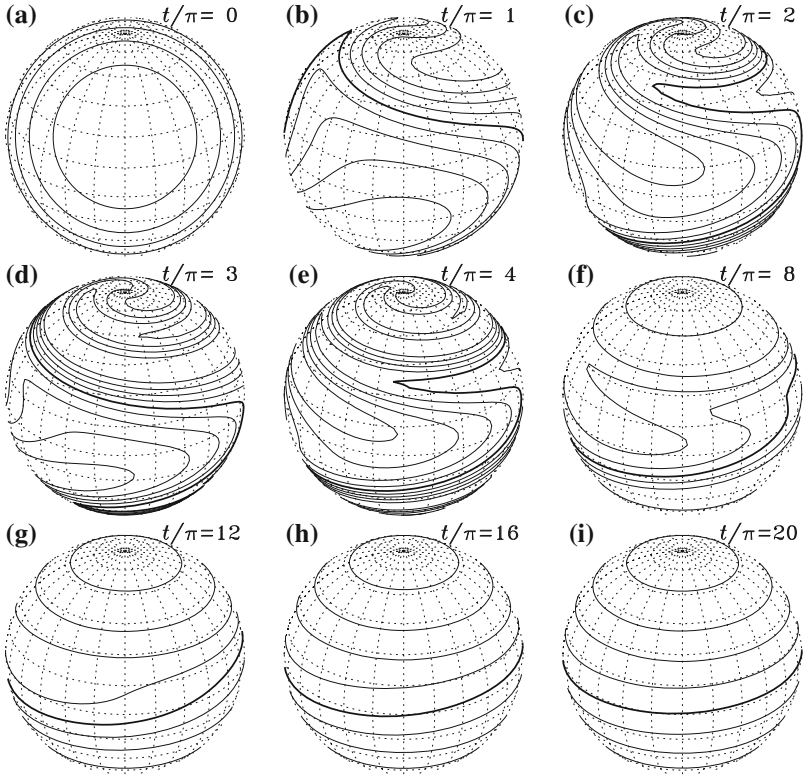

Fig. 2.13 Symmetrization of an inclined dipole in an electrically conducting sphere in a state of solar-like axisymmetric differential rotation. Each panel shows contours of constant B_r at the surface of the sphere, and the solution is matched to a potential in the exterior ($r/R > 1$). The differential rotation is given by Eq. (2.27). Time is given in units of $\tau_{\rm DR}$, in which the turnover period (or differential rotation period) is equal to 2π, and the magnetic Reynolds number is $\mathrm{R_m} = 10^3$.

But here is the amusing thing; for an observer looking at the magnetic field at the surface of the sphere, the enhanced decay of the perpendicular component of the dipole will translate into a gradual decrease in the inferred tilt axis of the dipole. Figure 2.13 shows this effect, for the differential rotation profile given by Eq. (2.27) and a magnetic Reynolds number $\mathrm{R_m} = 10^3$. Contours of constant B_r are plotted on the surface $r/R = 1$, with the neutral line ($B_r = 0$) plotted as a thicker line. At $t = 0$ the field has the form of a pure dipole tilted by $\pi/3$ with respect to the coordinate axis, and the sphere is oriented so that the observer (you!) is initially looking straight down the magnetic axis of the dipole. Advection by the flow leads to a distortion of the initial field, with the subsequent buildup of small spatial scales in the r- and

θ-directions (only the latter can be seen here).[6] After only two turnover times (last frame), the surface field looks highly axisymmetric.

So, in a differentially rotating fluid system with high R_m, flux expulsion leads to the *symmetrization* of any non-axisymmetric magnetic field component initially present—or contemporaneously generated. The efficiency of the symmetrization process should make us a little cautious in assuming that the large-scale magnetic field of the sun, which one would deem roughly axisymmetric upon consideration of surface things like the sunspot butterfly diagram, is characterized by the same level of axisymmetry in the deep-seated generating layers, where the dynamo is presumed to operate. After all, standing in between is a thick, axisymmetrically differentially rotating convective envelope that must be reckoned with. In fact, observations of coronal density structures in the descending phase of the solar cycle can be interpreted in terms of a large-scale, tilted dipole component, with the tilt angle steadily decreasing over 3–4 years towards solar minimum. Interestingly, the differential rotation timescale for the sun is ~ 6 months. Are we seeing the axisymmetrization process in operation? Maybe. Axisymmetry is certainly a very convenient modelling assumption when working on the large scales of the solar magnetic field, but it may be totally wrong.

Axisymmetrization has also been invoked as an explanation for the almost perfectly axisymmetric magnetic field of the planet Saturn, which stands in stark contrast to the other solar system planetary magnetic fields. Saturn has a very pronounced surface latitudinal differential rotation, characterized by equatorial acceleration, and current structural models suggest that this differential rotation may persist in the molecular Hydrogen envelope, down to the edge of the metallic Hydrogen core ($r/R_S \simeq 0.55$), where dynamo action is presumed to take place. This would be an ideal configuration for axisymmetrization of a non-axisymmetric deep magnetic field, provided the electrical conductivity is high enough at the base of the envelope to ensure good coupling between the magnetic field and the fluid.

2.4 Two Anti-Dynamo Theorems

The cellular flow studied in Sect. 2.3, although it initially looked encouraging (cf. Fig. 2.9), proved not to be a dynamo after all. Is this peculiar to the flow defined by Eqs. (2.34)–(2.35), or is this something more general? Exhaustively testing for dynamo action in all possible kinds of flow geometries is clearly impractical. However, it turns out that one can rule out a priori dynamo action in many classes of flows. These demonstrations are known as *anti-dynamo theorems*.

[6] An animation of this solution, as well as a few others for different R_m and/or tilt angle, can be viewed on the course web-page.

2.4.1 Zeldovich's Theorem

A powerful anti-dynamo theorem due to Zeldovich (1914–87), has a lot to teach us about our cellular flow results. The theorem rules out dynamo action in incompressible ($\nabla \cdot \boldsymbol{u} = 0$) steady planar flows in cartesian geometry, i.e., flows of the form

$$\boldsymbol{u}_2(x, y, z) = u_x(x, y, z)\hat{\boldsymbol{e}}_x + u_y(x, y, z)\hat{\boldsymbol{e}}_y \tag{2.52}$$

in a bounded volume V at the boundaries (∂V) of which the magnetic field vanishes. Note that no other restrictions are placed on the magnetic field, which can depend on all three spatial coordinate as well as time. Nonetheless, in view of Eq. (2.52) it will prove useful to consider the z-component of the magnetic field $B_z(x, y, z, t)$ separately from the (2D) field component in the $[x, y]$ plane (hereafter denoted $\boldsymbol{B}_2$). It is readily shown that the z-component of the induction equation then reduces to

$$\left(\frac{\partial}{\partial t} + \boldsymbol{u} \cdot \nabla\right) B_z = \eta \nabla^2 B_z \tag{2.53}$$

for spatially constant magnetic diffusivity. Now, the LHS is just a Lagrangian derivative, yielding the time variation of B_z as one moves along with the fluid. Multiplying this equation by B_z and integrating over V yields, after judicious use of Green's first identity (see Appendix A):

$$\frac{1}{2}\int_V \frac{\mathrm{D}B_z^2}{\mathrm{D}t}\,\mathrm{d}V = \eta \int_{\partial V} B_z(\nabla B_z) \cdot \boldsymbol{n}\,\mathrm{d}S - \eta \int_V (\nabla B_z)^2 \mathrm{d}V\ . \tag{2.54}$$

Now, the first integral on the RHS vanishes since $\boldsymbol{B} = 0$ on ∂V by assumption. The second integral is positive definite, *therefore B_z always decays on the diffusive timescale* (cf. Sect. 2.1).

Consider now the magnetic field $\boldsymbol{B}_2$ in $[x, y]$ planes. The most general such 2D field can be written as the sum of a solenoidal and potential component:

$$\boldsymbol{B}_2(x, y, z, t) = \nabla \times (A\hat{\boldsymbol{e}}_z) + \nabla \Phi\ , \tag{2.55}$$

where the vector potential A and scalar potential Φ both depend on time and on all three spatial coordinates, except for Φ having no z-dependency. The constraint $\nabla \cdot \boldsymbol{B} = 0$ then implies

$$\nabla_2^2 \Phi = -\frac{\partial B_z}{\partial z}\ , \tag{2.56}$$

where $\nabla_2^2 \equiv \partial^2/\partial x^2 + \partial^2/\partial y^2$ is the 2D Laplacian operator in the $[x, y]$ plane. Clearly, once B_z has resistively dissipated, i.e., for times much larger than the global resistive decay time τ_η, Φ is simply a solution of the 2D Laplace equation $\nabla_2^2 \Phi = 0$.

Here comes the sneaky part. We first substitute Eq. (2.55) into the induction (1.59), and then take the curl of the resulting expression; this last manoeuvre will lead to the disappearance of all but one contribution from the $\nabla\Phi$ term, since $\nabla \times \nabla\Phi = 0$ identically. Moreover, since $\boldsymbol{u}_2$ and $A\hat{\boldsymbol{e}}_z$ are here orthogonal by construction, we also have $\boldsymbol{u}_2 \times \nabla \times (A\hat{\boldsymbol{e}}_z) = -(\boldsymbol{u}_2 \cdot \nabla)(A\hat{\boldsymbol{e}}_z)$. Since the time and spatial derivatives commute, a bit of vector algebra allows to write the remaining terms in the form:

$$\nabla \times \nabla \times \left[\frac{\partial (A\hat{\boldsymbol{e}}_z)}{\partial t} + \boldsymbol{u}_2 \cdot \nabla (A\hat{\boldsymbol{e}}_z) - \eta \nabla_2^2 (A\hat{\boldsymbol{e}}_z) - \boldsymbol{u}_2 \times \nabla\Phi \right] = 0 \,, \tag{2.57}$$

with $\nabla \cdot (A\hat{\boldsymbol{e}}_z) = 0$ as a choice of gauge. In general, the above expression is only satisfied if the quantity in square brackets itself vanishes, i.e.,

$$\left(\frac{\partial}{\partial t} + \boldsymbol{u}_2 \cdot \nabla \right) A = \eta \nabla_2^2 A + (\boldsymbol{u}_2 \times \nabla\Phi) \cdot \hat{\boldsymbol{e}}_z \,. \tag{2.58}$$

This expression is identical to that obtained above for B_z, except for the presence of the source term $\boldsymbol{u}_2 \times \nabla\Phi$. However, we just argued that for $t \gg \tau_\eta$, $\nabla_2^2 \Phi = 0$. In addition, $\boldsymbol{B}$ vanishes on ∂V by assumption, so that the only possible asymptotic interior solutions are of the form Φ =const, which means that the source term vanishes in the limit $t \gg \tau_\eta$. From this point on Eq. (2.58) is indeed identical to Eq. (2.53), for which we already demonstrated the inevitability of resistive decay. Therefore, dynamo action, i.e., maintenance of a magnetic field against resistive dissipation, is impossible in a planar flow for *any* 3D magnetic field.

2.4.2 Cowling's Theorem

Another powerful anti-dynamo theorem, predating in fact Zeldovich's, is due to Cowling (1906–90). This anti-dynamo theorem is particularly important historically, since it rules out dynamo action for 3D but axisymmetric flows and magnetic fields, which happen to be the types of flows and fields one sees in the sun, at least on the larger spatial scales. Rather than going over one of the many formal proofs of Cowling's theorem found in the literature, let's just follow the underlying logic of our proof of Zeldovich's theorem.

Assuming once again that there are no sources of magnetic field exterior to the domain boundaries, we consider the inductive action of a 3D, steady axisymmetric flow on a 3D axisymmetric magnetic field. Working in spherical polar coordinates (r, θ, ϕ), we write:

$$\boldsymbol{u}(r,\theta) = \frac{1}{\varrho} \nabla \times (\Psi(r,\theta)\hat{\boldsymbol{e}}_\phi) + \varpi\Omega(r,\theta)\hat{\boldsymbol{e}}_\phi \,, \tag{2.59}$$

$$\boldsymbol{B}(r,\theta,t) = \nabla \times (A(r,\theta,t)\hat{\boldsymbol{e}}_\phi) + B(r,\theta,t)\hat{\boldsymbol{e}}_\phi \,, \tag{2.60}$$

where $\varpi = r \sin\theta$. Here, the azimuthal vector potential A and stream function Ψ define the poloidal components of the field and flow, and Ω is the angular velocity (units rad s^{-1}). Note that the form of Eq. (2.59) guarantees that $\nabla \cdot (\varrho \boldsymbol{u}) = 0$, describing mass conservation in a steady flow. Separation of the (vector) MHD induction equation into two components for the 2D scalar fields A and B, as done in Sect. 2.1, now leads to:

$$\left(\frac{\partial}{\partial t} + \boldsymbol{u}_p \cdot \nabla\right)(\varpi A) = \varpi\eta\left(\nabla^2 - \frac{1}{\varpi^2}\right) A \ , \tag{2.61}$$

$$\left(\frac{\partial}{\partial t} + \boldsymbol{u}_p \cdot \nabla\right)\left(\frac{B}{\varpi}\right) = \frac{\eta}{\varpi}\left(\nabla^2 - \frac{1}{\varpi^2}\right) B + \frac{1}{\varpi^2}\frac{\mathrm{d}\eta}{\mathrm{d}r}\frac{\partial(\varpi B)}{\partial r} - \left(\frac{B}{\varpi}\right)\nabla \cdot \boldsymbol{u}_p + \boldsymbol{B}_p \cdot \nabla\Omega \ , \tag{2.62}$$

where $\boldsymbol{B}_p$ and $\boldsymbol{u}_p$ are notational shortcuts for the poloidal field and meridional flow. Notice that the vector potential A evolves in a manner entirely independent of the toroidal field B, the latter being conspicuously absent on the RHS of Eq. (2.61). This is not true of the toroidal field B, which is well aware of the poloidal field's presence via the $\nabla\Omega$ shearing term.

The LHS of these expressions is again a Lagrangian derivative for the quantities in parentheses, and the first terms on each RHS are of course diffusion. The next term on the RHS of Eq. (2.62) vanishes for incompressible flows, and remains negligible for very subsonic compressible flows. The last term on the RHS, however, is a source term, in that it can lead to the growth of B *as long as* A *does not decay away*. This is the very situation we have considered in Sect. 2.2.4, by holding A fixed as per Eq. (2.23). However, there is no similar source-like term on the RHS of Eq. (2.61), which governs the evolution of A.

This should now start to remind you of Zeldovich's theorem. In fact, Eq. (2.3) is structurally identical to Eq. (2.53), for which we demonstrated the inevitability of resistive decay in the absence of sources exterior to the domain. This means that A will inexorably decay, implying in turn that B will then also decay once A has vanished. Since axisymmetric flows cannot maintain A against Ohmic dissipation, *a 3D axisymmetric flow cannot act as a dynamo for a 3D axisymmetric magnetic field*.[7] Cowling's theorem is not restricted to spherical geometry, and is readily generalized to any situation where both flow and field showing translational symmetry in one and the same spatial coordinate. Such physical systems are said to have an *ignorable coordinate*.

It is worth pausing and reflecting on what these two antidynamo theorems imply for the cellular flow of Sect. 2.3. It was indeed a planar flow ($u_z = 0$), and moreover the magnetic field had an ignorable coordinate ($\partial \boldsymbol{B}/\partial z \equiv 0$)! We thus fell under the

[7] A fact often unappreciated is that Cowling's theorem does not rule out the dynamo generation of a *non-axisymmetric* 3D magnetic field by a 3D axisymmetric flow.

purview of both Zeldovich's and Cowling's theorems, so in retrospect our failure to find dynamo action is now understood.

2.5 The Roberts Cell Dynamo

Clearly, the way to evade both theorems is to consider flows and fields that are fully three-dimensional, and lack translational symmetry in either the flow or the magnetic field. We now consider one such flow, and examine some of its dynamo properties.

2.5.1 The Roberts Cell

The Roberts cell is a spatially periodic, incompressible flow defined over a 2D domain $(x, y) \in [0, 2\pi]$ in terms of a stream function

$$\Psi(x, y) = \cos x + \sin y \ , \tag{2.63}$$

so that

$$\boldsymbol{u}(x, y) = \frac{\partial \Psi(x, y)}{\partial y}\hat{\boldsymbol{e}}_x - \frac{\partial \Psi(x, y)}{\partial x}\hat{\boldsymbol{e}}_y + \Psi(x, y)\hat{\boldsymbol{e}}_z \ . \tag{2.64}$$

Note that the flow velocity is independent of the z-coordinate, even though the flow has a non-zero z-component. Equations (2.63)–(2.64) describe a periodic array of counterrotating flow cells in the $[x, y]$ plane, with a z-component that changes sign from one cell to the next; the total flow is then a series of helices, which have the same kinetic helicity $h = \boldsymbol{u} \cdot \nabla \times \boldsymbol{u}$ in each cell. The Roberts cell flow represents one example of a *Beltrami flows*, i.e., it satisfies the relation $\nabla \times \boldsymbol{u} = \alpha \boldsymbol{u}$, where α is a numerical constant. Such flows are *maximally helical*, in the sense that their vorticity ($\boldsymbol{\omega} \equiv \nabla \times \boldsymbol{u}$) is everywhere parallel to the flow, which maximizes helicity for a given flow speed. Figure 2.14 shows one periodic "unit" of the the Roberts cell flow pattern. Take note already of the presence of stagnation points where the corners of four contiguous flow cells meet.

Let's first pause and consider why one should expect the Roberts cell to evade Cowling's and Zeldovich's theorems. First, note that this is not a planar flow in the sense demanded by Zeldovich's theorem, since we do have three non-vanishing flow components. However, the z-coordinate is ignorable in the sense of Cowling's theorem, since all flow components are independent of z. *If this flow is to evade Cowling's theorem and act as a dynamo, it must act on a magnetic field that is dependent on all three spatial coordinates.*

Consequently, we consider the inductive effects of this flow acting on a fully three dimensional magnetic field $\boldsymbol{B}(x, y, z, t)$. Since the flow speed is independent of z, we can expect solutions of the linear induction equation to be separable in z, i.e.:

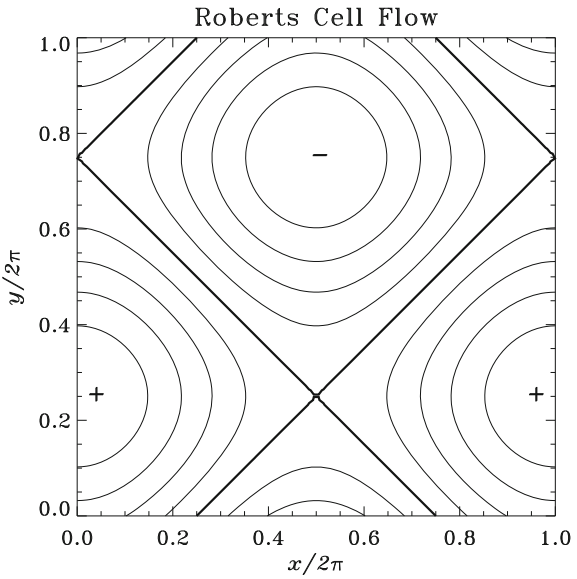

Fig. 2.14 The Roberts cell flow. The flow is periodic in the $[x, y]$ plane, and independent of the z-coordinate (but $u_z \neq 0$!). Flow streamlines are shown projected in the $[x, y]$ plane, and the $+/-$ signs indicate the direction of the z-component of the flow. The *thicker contour* defines the network of *separatrix surfaces* in the flow, corresponding to cell boundaries and intersecting at stagnation points. The $u_z(x, y)$ isocontours coincide with the projected streamlines.

$$\boldsymbol{B}(x, y, z, t) = \boldsymbol{b}(x, y, t)e^{ikz} \,, \tag{2.65}$$

where k is a (specified) wave vector in the z-direction, and the 2D magnetic amplitude $\boldsymbol{b}$ is now a complex quantity. We are still dealing with a fully 3D magnetic field, but the problem has been effectively reduced to two spatial dimensions (x, y), which represents a great computational advantage.

2.5.2 Dynamo Solutions

From the dynamo point of view, the idea is again to look for solutions of the induction equations where the magnetic energy does not fall to zero as $t \to \infty$. In practice this means specifying k, as well as some weak field as an initial condition, and solve the 2D linear initial value problem for $\boldsymbol{b}(x, y, t)$ resulting from the substitution of Eq. (2.65) into the induction equation:

$$\frac{\partial \boldsymbol{b}}{\partial t} = (\boldsymbol{b} \cdot \nabla_{xy})\boldsymbol{u} - (\boldsymbol{u} \cdot \nabla_{xy})\boldsymbol{b} - iku_z\boldsymbol{b} + \mathrm{R}_\mathrm{m}^{-1}(\nabla_{xy}^2\boldsymbol{b} - k^2\boldsymbol{b}) \,, \tag{2.66}$$

subjected to periodic boundary conditions on $\boldsymbol{b}$, in order to avoid the potentially misleading role of fixed-flux boundary conditions in driving dynamo action, as encountered in Sect. 2.3. Here ∇_{xy} and ∇_{xy}^2 are the 2D gradient and Laplacian operators in the $[x, y]$ plane. As before we use as a time unit the turnover time τ_c, which

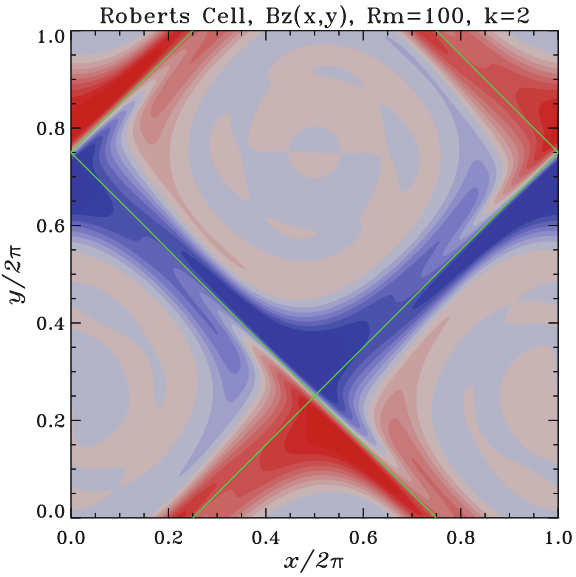

Fig. 2.15 Isocontours for the z-component of the magnetic field in the $[x, y]$ plane, for Roberts cell dynamo solutions with $\mathrm{R_m} = 100$ and $k = 2$, in the asymptotic regime $t \gg \tau_c$. The color scale codes the real part of the z-component of $\boldsymbol{b}(x, y, t)$ (*gray-to-blue* is negative, *gray-to-red* positive). The *green straight lines* indicate the separatrix surfaces of the flow (see Fig. 2.14). Note the flux expulsion from the cell centers, and the concentration of the magnetic flux in thin sheets pressed against the separatrices. In the $t \gg \tau_c$ regime, the field grows exponentially but the shape of the planform is otherwise steady. Compare this with Fig. 2.12b.

is of order 2π here. All solutions described below were again obtained numerically, starting from a weak, horizontal magnetic field as the initial condition.

The time evolution can be divided into three more or less distinct phases, the first two being similar to the case of the 2D cellular flow considered in Sect. 2.3: (1) quadratic growth of the magnetic energy for $t \lesssim \tau_c$; (2) flux expulsion for the subsequent few τ_c. However, and unlike the case considered in Sect. 2.3, for some values of k the third phase is one of *exponential growth* in the magnetic field (and energy).

Figure 2.15 shows a typical Roberts cell dynamo solution, for $\mathrm{R_m} = 10^2$ and $k = 2$. What is plotted is the real part of the z-component of $\boldsymbol{b}(x, y, t)$, at time $t \gg \tau_c$. The thick green lines are the separatrices of the flow. One immediately recognizes the workings of flux expulsion, in that very little magnetic flux is present near the center of the flow cells. Instead the field is concentrated in boundary-layer-like thin sheets parallel to the separatrix surfaces. Given our extensive discussion of flux expulsion in Sect. 2.3, it should come as no surprise that the thickness of those sheets scales as $\mathrm{R_m}^{-1/2}$. For $t \gg \tau_c$, the field grows exponentially, but the shape of the "planform" remains fixed. In other words, even though we solved the induction

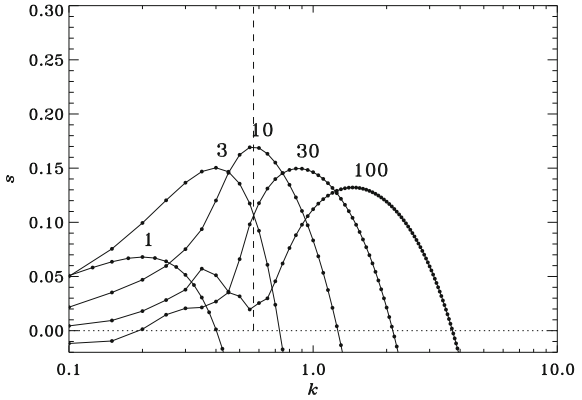

Fig. 2.16 Growth rates of the magnetic energy in the Roberts cell, for sequences of solutions with increasing k and various values of $\mathrm{R_m}$, as labeled near the maxima of the various curves. Growth typically occurs for a restricted range in k, and peaks at a value $k_{\max}$ that increases slowly with increasing $\mathrm{R_m}$. Note however how the corresponding maximum growth rate decreases with increasing $\mathrm{R_m}$. The small "dip" left of the main peaks for the high-$\mathrm{R_m}$ solutions is a real feature, although here it is not very well resolved in k.

equation as an initial value problem, the solution can be thought of as an eigensolution of the form $\boldsymbol{B}(x, y, z, t) = \boldsymbol{b}(x, y)e^{ikz+st}$, with $\mathrm{Re}(s) > 0$ and $\mathrm{Im}(s) = 0$.

In terms of the magnetic energy evolution, the growth rate s of $\boldsymbol{b}(x, y, t)$ is readily obtained by a linear least-squares fit to the $\log \mathcal{E}_B$ versus t curves in the $t \gg \tau_c$ regime, or more formally defined as

$$s = \lim_{t\to\infty} \left[\frac{1}{2t} \log(\mathcal{E}_B) \right]. \tag{2.67}$$

It turns out that the Roberts cell flows yields dynamo action (i.e., $s > 0$) over wide ranges of wave numbers k and magnetic Reynolds number $\mathrm{R_m}$. Figure 2.16 shows the variations in growth rates with k, for various values of $\mathrm{R_m}$. The curves peak at a growth rate value $k_{\max}$ that gradually shifts to higher k as $\mathrm{R_m}$ increases. The largest growth rate is $k_{\max} \simeq 0.17$, and occurs at $\mathrm{R_m} \simeq 10$. It can be shown (see bibliography) that in the high $\mathrm{R_m}$ regimes the following scalings hold:

$$k_{\max} \propto \mathrm{R_m}^{1/2}, \qquad \mathrm{R_m} \gg 1\ , \tag{2.68}$$

$$s(k_{\max}) \propto \frac{\log(\log \mathrm{R_m})}{\log \mathrm{R_m}}, \qquad \mathrm{R_m} \gg 1\ . \tag{2.69}$$

To understand the origin of these peculiar scaling relations, we need to take a closer look at the mechanism through which the magnetic field is amplified by the Roberts cell.

2.5.3 Exponential Stretching and Stagnation Points

Even cursory examination of Fig. 2.15 suggests that magnetic field amplification in the Roberts cell is somehow associated with the network of separatrices and stagnation points. It will prove convenient in the foregoing analysis and discussion to first introduce new coordinates:

$$x' = x - y \ , \qquad y' = x + y + \frac{3\pi}{2} \ , \tag{2.70}$$

corresponding to a $3\pi/2$ translation in the y-direction, followed by 45° rotation about the origin in the $[x, y]$ plane. The separatrices are now parallel to the coordinate lines $x' = n\pi$, $y' = n\pi$ ($n = 0, 1, ...$), and the stream function has become

$$\Psi(x', y') = 2\sin(x')\sin(y') \ . \tag{2.71}$$

Close to the stagnation points, a good approximation to Eq. (2.71) is

$$\Psi(x', y') \simeq 2x'y' \ , \qquad x', y' \ll 1 \ , \tag{2.72}$$

which, if anything else, should now clarify why this is called a hyperbolic stagnation point... Consider now a fluid element flowing in the vicinity of this stagnation point. From a Lagrangian point of view its equations of motion are:

$$\frac{\partial x'}{\partial t} = u_{x'} = 2x' \ , \tag{2.73}$$

$$\frac{\partial y'}{\partial t} = u_{y'} = -2y' \ , \tag{2.74}$$

which immediately integrates to

$$x'(t) = x'_0 e^{2t}, \qquad y'(t) = y'_0 e^{-2t} \ , \tag{2.75}$$

where (x'_0, y'_0) is the location of the fluid element at $t = 0$. Evidently, the fluid element experiences *exponential stretching* in the x'-direction, and corresponding contraction in the y'-direction (since $\nabla \cdot \boldsymbol{u} = 0$!). Now, recall that in ideal MHD ($\mathrm{R_m} = \infty$) a magnetic fieldline obeys an equation identical to that of a line element, and that stretching leads to field amplification as per the mass conservation constraint (Sect. 2.2.1). Clearly, stagnation points have quite a bit of potential, when it comes to amplifying exponentially a pre-existing magnetic field... provided diffusion and destructive folding can be held at bay. Let's look into how this is achieved in the Roberts Cell.

2.5.4 Mechanism of Field Amplification in the Roberts Cell

We stick to the rotated Roberts cell used above, restrict ourselves to the $R_m \gg 1$ regime, and pick up the field evolution after flux expulsion is completed and the magnetic field is concentrated in thin boundary layers (thickness $\propto R_m^{-1/2}$) pressed against the separatrices (as on Fig. 2.15).

Consider a x'-directed magnetic fieldline crossing a vertical separatrix, as shown on Fig. 2.17a (gray line labeled "a"). The y' component of the flow is positive on either side of the separatrix, and peaks on the separatrix. Consequently, the fieldline experiences stretching in the y'-direction ($a \to b \to c \to d$ on Fig. 2.17a). However, the induced y' component of the magnetic field changes sign across the separatrix, so that we seem to be heading towards our dreaded destructive folding. This is where the crucial role of the vertical (z) dimension becomes apparent. Figure 2.17b is a view of the same configuration in the $[x', z]$ plane, looking down onto the y' axis on part A. At $t = 0$ the fieldlines have no component in the z-direction, but in view of the assumed e^{ikz} spatial dependency the x' component changes sign every half-wavelength k/π. Consider now the inductive action of the z-component of the velocity, which changes sign across the separatrix. After some time interval of order $k/(\pi u_z)$ the configuration

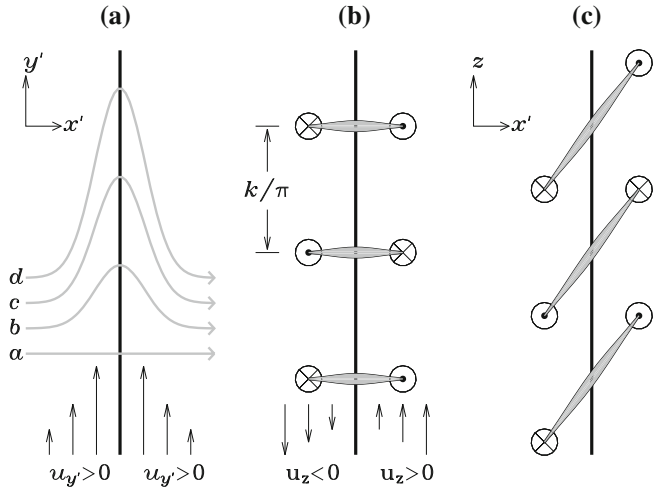

Fig. 2.17 Mechanism of magnetic field amplification in the Roberts cell flow. The diagram is plotted in terms of the rotated $[x', y']$ Roberts cell. The *thick vertical line* is a separatrix surface, and the *gray lines* are magnetic fieldlines. Part **a** is a view in the horizontal plane $[x', y']$, and shows the production of a y'-directed magnetic component from an initially x'-directed magnetic field (line labeled "a"). Parts **b** and **c** are views in the $[x', z]$ plane looking down along the y' axis, and illustrate the phase shift in the z-direction of the y' magnetic component caused by the z-component of the velocity. The symbol $\odot$ ($\otimes$) indicates a magnetic field coming out (into) the plane of the page. Note on part (**c**) how footpoints of identical polarity are brought in close proximity, thus avoiding the destructive folding that would have otherwise characterized the situation depicted on part (**b**) in the $u_z = 0$ 2D case.

of Fig. 2.17b will have evolved to that shown on part C. Observe what has happened: the fieldlines have been sheared in such a way that y'-components of the magnetic field of like signs have been brought in close proximity. Contrast this to the situation on part B, where magnetic footpoints in closest proximity have oppositely directed y'-components.

The end result of this process is that a y'-directed magnetic field is produced by shearing of the initial x'-directed field, with a phase shift in the z-direction such that destructive folding is avoided. Clearly, this requires *both* a z-component of velocity, *and* a z-dependency in the magnetic field. Either alone won't do the trick.

Now, the same reasoning evidently applies to a y'-directed magnetic fieldline crossing a horizontal separatrix: a x'-directed magnetic field will be induced. That magnetic field will be swept along the horizontal separatrix, get further amplified by exponential stretching as it zooms by the stagnation point, and continue along the vertical separatrix, where it can now serve as a seed field for the production of a y'-directed field. The dynamo "loop" is closed, at any time the rate of field production is proportional to the local field strength, and exponential growth of the field follows. The process works best if the half wavelength k/π is of order of the boundary layer thickness, which in fact is what leads to the scaling law given by Eq. (2.68). The scaling for the growth rate (Eq. 2.69), in turn, is related to the time spent by a fluid element in the vicinity of the stagnation point.

2.5.5 *Fast Versus Slow Dynamos*

One worrisome aspect of the Roberts cell dynamo is the general decrease of the growth rates with increasing $\mathrm{R_m}$ (see Fig. 2.16); worrisome, because the $\mathrm{R_m} \to \infty$ limit is the one relevant to most astrophysically interesting circumstances. A dynamo exhibiting this property is called a *slow dynamo*, in contrast to a *fast dynamo*, which (by definition) retains a finite growth rate as $\mathrm{R_m} \to \infty$, the formal requirement being that

$$\lim_{\mathrm{R_m}\to\infty} s(k_{\max}) > 0 \,. \tag{2.76}$$

In view of Eq. (2.69), the Roberts cell is thus formally a slow dynamo. However the RHS of Eq. (2.69) is such a slowly decreasing function of $\mathrm{R_m}$ that the Roberts cell is arguably the closest thing it could be to a fast dynamo... without formally being one.

The distinction hinges on the profound differences between the strict mathematical case of $\mathrm{R_m} = \infty$ (ideal MHD), and the more physically relevant limit $\mathrm{R_m} \to \infty$. From the physical point of view, the distinction is a crucial one. One example will suffice. Recall that in the absence of dissipation magnetic helicity is a conserved quantity in any evolving magnetized fluid:

$$\frac{\mathrm{d}\mathcal{H}_B}{\mathrm{d}t} = \frac{\mathrm{d}}{\mathrm{d}t}\int_V \boldsymbol{A}\cdot\boldsymbol{B}\,\mathrm{d}V = 0, \tag{2.77}$$

where $\boldsymbol{B} = \nabla\times\boldsymbol{A}$. Dynamo action, in the sense of amplifying a weak initial field, is then clearly impossible except for the subset of initial fields having $\mathcal{H}_B = 0$. This is a very stringent constraint on dynamo action! Go back now to the Roberts cell dynamo in the high-$\mathrm{R_m}$ regime. We saw that magnetic structures build up on a horizontal length scale $\propto \mathrm{R_m}^{-1/2}$, and that the vertical wavelength of the fastest growing mode also decreases as $\mathrm{R_m}^{-1/2}$. *The inexorable shrinking of the length scales ensures that dissipation always continue to operate even in the* $\mathrm{R_m}\to\infty$ *limit*. This is why the Roberts cell dynamo can evade the constraint of helicity conservation. This is also why it is a slow dynamo. On the other hand, the Vainshtein & Zeldovich Stretch–Twist–Fold dynamo of Sect. 2.2, with its growth rate $\sigma = \ln 2$, is a fast dynamo since nothing prevents it from operating in the $\mathrm{R_m}\to\infty$ limit.

But is this really the case? In the flows we have considered up to now, the existence of dynamo action hinges on stretching winning over destructive folding; in the 2D cellular flow of Sect. 2.3, destructive folding won over stretching everywhere away from boundaries. In the Roberts cell, destructive folding is avoided only for vertical wave numbers such that magnetic fields of like signs are brought together, minimizing dissipation. The STF dynamo actually combines stretching and constructive folding, such that folding *reinforces* stretching. The fact that destructive folding is avoided entirely is why the growth rate does not depend on $\mathrm{R_m}$.

Well, upon further consideration it turns out that magnetic diffusivity must play a role in the STF rope dynamo after all. Diffusion comes in at two levels; the first and most obvious one is at the "crossings" formed by the STF sequence. The second and less obvious arises from the fact that as one applies the STF operation n times, the resulting "flux rope" is in fact made up of n closely packed flux ropes, each of cross-section $\propto 2^{-n}$ times smaller than the original circular flux rope, so that the total cross-section looks more like a handful of spaghettis that it does a single monolithic flux rope of strength $\propto 2^n$. If one waits long enough, the magnetic length scale perpendicular to the loop axis shrinks to zero, so that even in the $\mathrm{R_m}\to\infty$ limit dissipation is bound to come into to play.

2.6 The CP Flow and Fast Dynamo Action

It turns out that a simple modification of the Roberts cell flow can turn it into a true fast dynamo. The so-called CP flow (for "Circularly Polarized") is nothing more that the original Roberts cell flow, with a forced time-dependence. It is once again a spatially periodic, incompressible flow, defined in cartesian coordinate over a 2D domain $(x, y) \in [0, 2\pi]$:

$$u_x(x, y, t) = A\cos(y + \varepsilon \sin \omega t), \tag{2.78}$$
$$u_y(x, y, t) = C\sin(x + \varepsilon \cos \omega t), \tag{2.79}$$
$$u_z(x, y, t) = A\sin(y + \varepsilon \sin \omega t) + C\cos(x + \varepsilon \cos \omega t). \tag{2.80}$$

Although the CP flow is not expressed here in terms of a stream function, this is the same as the Roberts Cell flow, except that now the counter-rotating flow cells are "precessing" in unison in the $[x, y]$ plane, along circular paths of radius ε, undergoing a full revolution in a time interval $2\pi/\omega$. Here and in what follows we set $\omega = 1$, $\varepsilon = 1$, $A = C = \sqrt{3/2}$, without any loss of generality.

2.6.1 Dynamo Solutions

The CP flow has the same spatial symmetry properties as the Roberts cell, and in particular is invariant in the z-direction. Consequently we again need to seek magnetic solutions with a z-dependency to evade Cowling's theorem. The magnetic field is again separable in z (Eq. 2.65), which leads to the 2D form of the induction equation already encountered with the Roberts cell (Eq. 2.66), subjected to periodic boundary conditions on $\boldsymbol{b}(x, y, t)$. As before, the idea is to pick a value for the vertical wavenumber k, and monitor dynamo action by tracking the growth (or decay) of the magnetic energy via Eq. (2.67).

Computing solutions for varying k soon reveals that dynamo action (i.e., positive growth rates $s(k, \mathrm{R_m})$) occurs in a finite range of vertical wavenumber k, with exponential growth setting in after a time of order of the turnover time. Figure 2.18 shows a snapshot of the vertical magnetic field $b_z(x, y, t)$ in this phase of exponential growth, for a $\mathrm{R_m} = 2000$ solution with $k = 0.57$, which here yields the largest growth rate. The solution is fully time-dependent, and its behavior is best appreciated by viewing it as an animation.[8]

The solution is characterized by multiple sheets of intense magnetic field, of thickness once again $\propto \mathrm{R_m}^{-1/2}$. The magnetic field exhibits *spatial intermittency*, in the sense that if one were to randomly choose a location somewhere in the $[x, y]$ plane, chances are good that only a weakish magnetic field would be found. In high-$\mathrm{R_m}$ solutions, strong fields are concentrated in small regions of the domain; in other words, their *filling factor* is small. This can be quantified by computing the *probability density function* (hereafter PDF) of the magnetic field strength, $f(|B_z|)$. This involves measuring B_z at every (x, y) mesh point in the solution domain, and simply counting how many mesh points have $|B_z|$ between values B and $B + \mathrm{d}B$. The result of such a procedure is shown in histogram form on Fig. 2.19. The PDF shows a power-law tail at high field strengths,

$$f(|B_z|) \propto |B_z|^{-\gamma}\,, \qquad |B_z| \gtrsim 10^{-5}\,, \tag{2.81}$$

[8] Which you can do, of course, on the course's web page, and for a few $\mathrm{R_m}$ values, moreover...

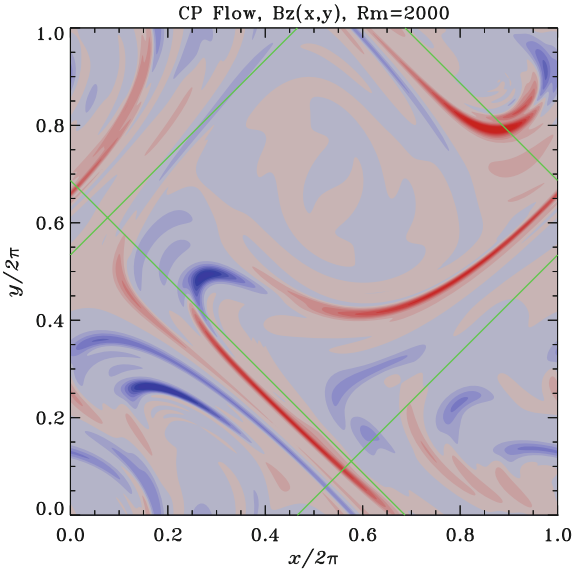

Fig. 2.18 Snapshot of the z-component of the magnetic field in the $[x, y]$ plane, for a CP flow solution with $\mathrm{R_m} = 2000$ and $k = 0.57$, in the asymptotic regime $t \gg \tau_c$. The color scale codes the real part of the z-component of $\boldsymbol{b}(x, y, t)$ (*gray-to-blue* is negative, *gray-to-red* positive). The *green straight lines* indicate the separatrix surfaces of the underlying pattern of flow cells, and are no longer fixed in space due to the precession of the flow cells (see Eqs. (2.78)–(2.80)). This is a strongly time-dependent solution, exhibiting overall exponential growth of the magnetic field.

spanning over four orders of magnitude in field strength, and with $\gamma \simeq 0.75$ here. This indicates that strong fields are still far more likely to be detected than if the magnetic field was simply a normally-distributed random variable (for example). The fact that the power law index γ is smaller than unity means that the *largest* local field strength found in the domain will always dominate the computation of the spatially-averaged field strength.

The CP flow dynamo solutions also exhibit *temporal intermittency*; if one sits at one specific point (x, y) in the domain and measures B_z at subsequent time steps, a weak B_z is measured most of the time, and only occasionally are large values detected. Once again the PDF shows a power-law tail with slope flatter than -1 indicating that a temporal average of B_z at one location will always be dominated by the largest B_z measured to date.

Unlike in the Roberts cell, the range of k yielding dynamo action does *not* shift significantly to higher k as $\mathrm{R_m}$ is increased, and in the high $\mathrm{R_m}$ regime the corresponding maximum growth rate $k_{\max}$ does *not* decrease with increasing $\mathrm{R_m}$ (as it does in Fig. 2.16). In the CP flow considered here ($A = C = \sqrt{3/2}$, $\omega = 1$, $\varepsilon = 1$), $k_{\max} \simeq 0.57$, with $s(k_{\max}) \simeq 0.3$ for $\mathrm{R_m} \gtrsim 10^2$, as shown on Fig. 2.20 (solid line). Figure 2.20 indicates that the CP flow operates as a fast dynamo.

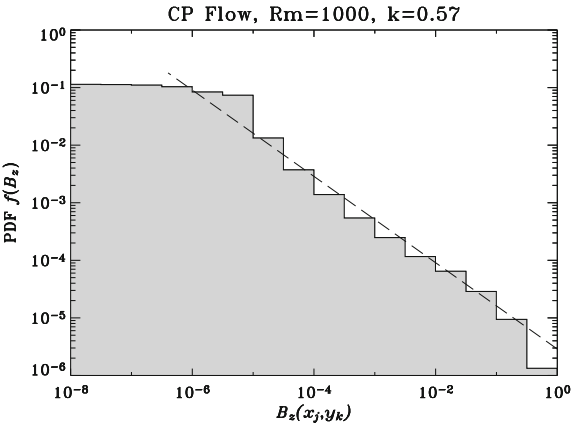

Fig. 2.19 Probability density function for the (unsigned) strength of the z-component of the magnetic field, for a $R_m = 10^3$, $k = 0.57$ CP flow dynamo. The peak field strength has been normalized to a value of unity. Note the power-law tail at large field strength (*straight line* in this log-log plot, with slope ~ -0.75).

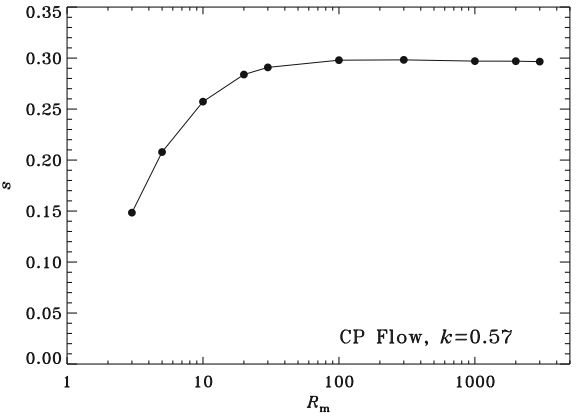

Fig. 2.20 Growth rate of $k = 0.57$ CP flow dynamo solutions, plotted as a function of the magnetic Reynolds number (*solid line*). The constancy of the growth rate in the high-R_m regime suggests (but does not strictly prove) that this dynamo is fast.

2.6.2 Fast Dynamo Action and Chaotic Trajectories

Fast dynamo action in the CP flow turns out to be intimately tied to the presence of *chaotic trajectories* in the flow. Their presence (or absence) in a given flow can be quantified in a number of ways, the most straightforward (in principle) being the calculations of the flow's *Lyapunov exponents*. This is another fancy name for a rather simple concept: the rate of exponential divergence of two neighbouring fluid element located at $\boldsymbol{x}_1$, $\boldsymbol{x}_2$ at $t = 0$ somewhere in the flow. The Lyapunov exponent λ_L can be (somewhat loosely) defined via

$$\ell(t) = \ell(0) \exp(\lambda_L t) \ , \tag{2.82}$$

where $\ell \equiv \|\boldsymbol{x}_2 - \boldsymbol{x_1}\|$ is the length of the *tangent vector* between the two fluid elements. Because there are three independent possible directions in 3D space, one can compute *three* distinct Lyapunov exponents at any given point in the flow, and it can be shown that for an incompressible flow their sum is zero. Now, recalling the

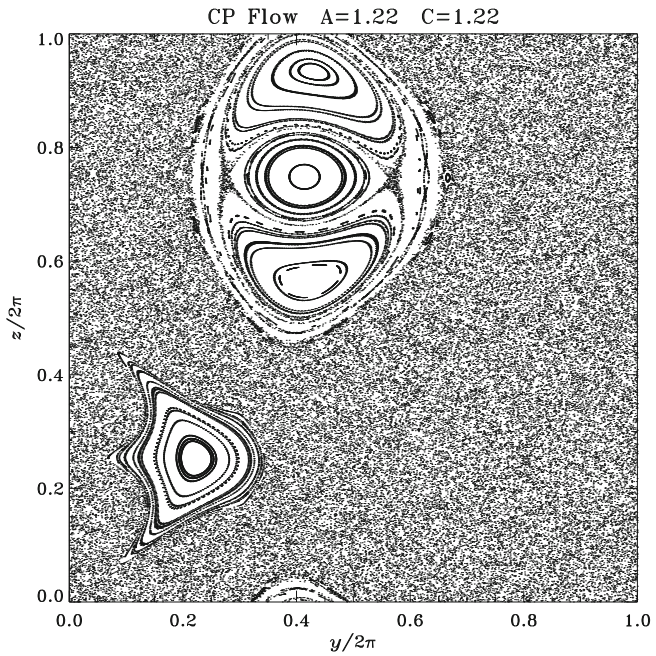

Fig. 2.21 Poincaré section for the CP flow, for $\varepsilon = 1$, $\omega = 1$, and $A = C = \sqrt{3/2}$. The plot is constructed by repeatedly "launching" particles at $z = 0$, $t = 0$, following their trajectories in time, and plotting their (projected) position (modulo 2π) in the $[x, y]$ plane at interval $\Delta t = 2\pi$. The flow is chaotic within the featureless "salt-and-pepper" regions, and integrable in regions threaded by closed curves.

simple flux tube stretching example of Sect. 2.2, exponential divergence of two points located in the same fieldline within the tube clearly implies exponential increase in the tube's length, and therefore, via Eq. (2.19), exponential increase of the magnetic field strength. Theorems have been proven, demonstrating that

1. A smooth flow cannot be a fast dynamo if $\lambda_L = 0$, so that $\lambda_L > 0$, or, equivalently, the existence of chaotic regions in the flow is a necessary (although not sufficient) condition for fast dynamo action;
2. In the limit $\mathrm{R_m} \to \infty$, the largest Lyapunov exponent of the flow is an upper bound on the dynamo growth rate.

Proofs of these theorems need not concern us here (if curious see bibliography), but they once again allow us to *rule out* fast dynamo action in many classes of flows.

Calculating a *Poincaré section*, as plotted on Fig. 2.21 for our CP flow, is another very useful way to check for chaotic trajectories in a flow. It is constructed by launching tracer particles at $z = 0$ (and $t = 0$), and following their trajectories as they are carried by the flow. At every 2π time interval, the position of each particle is plotted in the $[x, y]$ plane (modulo 2π in x and y, since most particles leave the original 2π-domain within which they were released as a consequence of cell precession).

Some particles never venture too far away from their starting position in the $[x, y]$ plane. They end up tracing closed curves which, however distorted they may end up looking, identify regions of space where trajectories are integrable. Other particles, on the other hand, never return to their starting position. If one waited long enough, one such particle would eventually come arbitrarily close to all points in the $[x, y]$ plane outside of the integrable regions. The corresponding particle trajectory is said to be *space filling*, and the associated particle motion chaotic. The region of the $[x, y]$ plane defined by the starting positions of all particles with space filling trajectories is called the *chaotic region* of the flow.

2.6.3 Magnetic Flux Versus Magnetic Energy

With the CP flow, we definitely have a pretty good dynamo on our hands. But how are those dynamo solutions to be related to the sun (or other astrophysical bodies)? So far we have concentrated on the magnetic energy as a measure of dynamo action, but in the astrophysical context *magnetic flux* is also important. Consider the following two (related) measures of magnetic flux:

$$\Phi = |\langle \boldsymbol{B} \rangle| \,, \qquad F = \langle |\boldsymbol{B}| \rangle \,, \tag{2.83}$$

where the angular brackets indicate some sort of suitable spatial average over the whole computational domain. The quantity Φ is nothing but the average magnetic flux, while F is the average *unsigned flux*. Under this notation the magnetic energy can be written as $\mathcal{E}_B = \langle \boldsymbol{B}^2 \rangle$.

Consider now the scaling of the two following ratios as a function of the magnetic Reynolds number:

$$\mathcal{R}_1 = \frac{\mathcal{E}_B}{\Phi^2} \propto \mathrm{R_m}^n \,, \tag{2.84}$$

$$\mathcal{R}_2 = \frac{F^2}{\Phi^2} \propto \mathrm{R_m}^\kappa \,. \tag{2.85}$$

A little reflection will reveal that a large value of $\mathcal{R}_1$ indicates that the magnetic field is concentrated in a small total fractional area of the domain, i.e., the *filling factor* is much smaller than unity.[9] The ratio $\mathcal{R}_2$, on the other hand, is indicative of the dynamo's ability to generate a net signed flux. The exponent κ measures the level of *folding* in the solution; large values of κ indicate that while the dynamo may be vigorously producing magnetic flux on small spatial scales, it does so in a manner such that very little *net* flux is being generated on the spatial scale of the computational domain. Figure 2.22 shows the variations with $\mathrm{R_m}$ of the two ratios defined above.

[9] If you can't figure it out try this: take a magnetic field of strength B_1 crossing a surface area A_1; now consider a more intense magnetic field, of strength $B_2 = 4B_1$, concentrated in one quarter of the area A_1; calculate $\mathcal{E}_B$, Φ, and $\mathcal{R}_1$... get it?

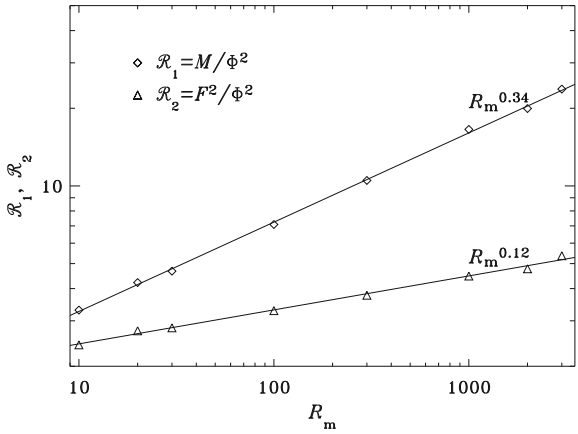

Fig. 2.22 Variations with R_m of the two ratios defined in Eqs. (2.84)–(2.85). Least squares fits (*solid lines*) yield power law exponents $n = 0.34$ and $\kappa = 0.12$.

Least squares fits to the curves yields $n = 0.34$ and $\kappa = 0.12$. Positive values for the exponents κ and n indicate that the CP flow dynamo is relatively inefficient at producing magnetic flux in the high R_m regime, and even less efficient at producing net signed flux. While other flows yielding fast dynamo action lead to different values for these exponents, in general they seem to always turn out positive, with $\kappa < n$, so that the (relative) inability to produce net signed flux seems to be a generic property of fast dynamos in the high-R_m regime.

2.6.4 Fast Dynamo Action in the Nonlinear Regime

We conclude this section by a brief discussion of fast dynamo action in the nonlinear regime. Evidently the exponential growth of the magnetic field will be arrested once the Lorentz force becomes large enough to alter the original CP flow. What might the nature of the backreaction on $\boldsymbol{u}$ look like?

Naively, one might think that the Lorentz force will simply reduce the amplitude of the flow components, leaving the overall geometry of the flow more or less unaffected. That this cannot be the case becomes obvious upon recalling that in the high R_m regimes the eigenfunction is characterized by magnetic structures of typical thickness $\propto R_m^{-1/2}$, while the flow has a typical length scale $\sim 2\pi$ in our dimensionless units. The extreme disparity between these two length scales in the high-R_m regime suggests that the saturation of the dynamo-generated magnetic field will involve alterations of the flow field on small spatial scales, so that a flow very much different from the original CP flow is likely to develop in the nonlinear regime.

That this is indeed what happens was nicely demonstrated some years ago by F. Cattaneo and collaborators (see references in the bibliography), who computed simplified nonlinear solutions of dynamo action in a suitably forced CP flow. They could show that

1. the r.m.s. flow velocity in the nonlinearly saturated regime is comparable to that in the original CP flow;
2. magnetic dissipation actually *decreases* in the nonlinear regime;
3. dynamo action is suppressed by the disappearance of chaotic trajectories in the nonlinearly modified flow.

2.7 Dynamo Action in Turbulent Flows

The Roberts cell and CP flow are arguably more akin to malfunctioning washing machines than any sensible astrophysical object. Nonetheless many things we have learned throughout this chapter do carry over to more realistic circumstances, and in particular to turbulent, thermally-driven convective fluid motions.

As support for this grand sweeping claim, consider Fig. 2.23 herein. It is a snapshot of a numerical simulation of dynamo action in a stratified, thermally-driven turbulent fluid being heated from below and spatially periodic in the horizontal directions. The fluid is contained in a rectangular box of aspect ratio $x : y : z = 10 : 10 : 1$, and we are here looking at the top layer of the simulation box, with the color scale encoding the vertical magnetic field component $B_z(x, y)$. Such thermally-driven turbulent flows in a stratified background have long been known to be characterized by cells of broad upwellings of warm fluid. These cells have a horizontal size set by, among other things, the density scale height within the box. On the other hand, the downwelling of cold fluid needed to satisfy mass conservation end up being concentrated in a network of narrow lanes at the boundaries between adjacent upwelling cells. This asymmetry is due to the vertical pressure and density gradient in the box: rising fluid expands laterally into the lower density layers above, and descending fluid is compressed laterally in the higher density layers below. Near the top of the simulation box, this leads to the concentration of magnetic structures in the downwelling lanes, as they are continuously being swept horizontally away from the centers of upwelling cells, through a form of flux expulsion in fact.

This convectively-driven turbulent flow acts as a vigorous nonlinear fast dynamo, with a ratio of magnetic to kinetic energy of about 20%. This dynamo, much like that arising in the CP flow, produces

1. magnetic fields that are highly intermittent, both spatially and temporally;
2. flux concentrations on scales $\propto \mathrm{R_m}^{-1/2}$;
3. little or no mean-field, i.e., signed magnetic flux on a spatial scale comparable to the size of the system.

The fundamental physical link between turbulent convection and the CP flow is the presence of chaotic trajectories in both flows, which leads to the expectation that dynamo action should be possible in convection zones of the sun and stars. Time to move on, then, to the solar magnetic field and its underlying dynamo mechanism(s).

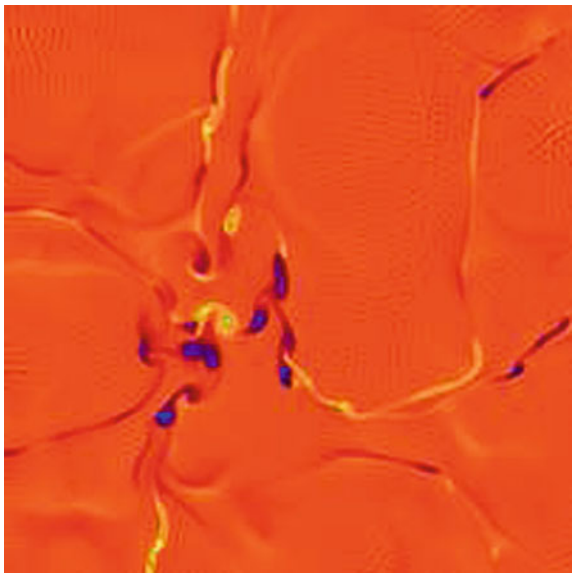

Fig. 2.23 Closeup on a snapshot of the top "horizontal" $[x, y]$ plane of a MHD numerical simulation of thermally-driven stratified turbulent convection in a box of aspect ratio $x : y : z = 10 : 10 : 1$, at a viscous Reynolds number of 245 and $\mathrm{R_m} = 1225$. The simulation uses a pseudo-spectral spatial discretization scheme, with 1024 collocation points in the x and y directions, and 97 in z. The color scale encodes the vertical (z) component of the magnetic field (*orange-to-yellow* is positive B_z, *orange-to-blue* negative). Numerical simulation results kindly provided by F. Cattaneo, University of Chicago.

Bibliography

The first detailed discussions of the diffusive decay of large-scale magnetic fields in astrophysical bodies are due to

Cowling, T. G.: 1945, *On the Sun's general magnetic field*, Mon. Not. Roy. Astron. Soc., **105**, 166–174

Wrubel, M. H.: 1952, *On the decay of a primeval stellar magnetic field*, Astrophys. J., **116**, 291–289

On the numerical solution of algebraic eigenvalue problems in general, and on inverse iteration in particular, see

Golub, G. H., & van Loan, C. F.: 1996, *Matrix Computations*, 3rd edn., The John Hopkins University Press, Sects. 7.6.1 and 7.7.8

Press, W. H., Teukolsky, S. A., Vetterling, W. T., & Flannery, B. P.: 1992, *Numerical Recipes. The Art of Scientific Computing*, 2nd edn., Cambridge University Press, Sect. 11.7

Chapter 19 of Press et al. also contains a good introduction to the art of PDE discretization by finite differences, including the simple explicit schemes used to compute the various solutions discussed in Sects. 2.3, 2.5 and 2.6.

Among the numerous books discussing the calculation of macroscopic transport coefficients

such as viscosity and electrical conductivity, starting from a microscopic point of view, I still like the following old classic:

Spitzer, Jr., L.: 1962, *Physics of Fully Ionized Gases*, 2nd edn., Wiley Interscience

On the Stretch-Twist-Fold dynamo, see

Vainshtein, S. I., & Zel'dovich, Y. B.: 1972, *Reviews of topical problems: origin of magnetic fields in astrophysics (turbulent "dynamo" mechanisms)*. Soviet Physics Uspekhi, **15**, 159–172

Moffatt, H. K., & Proctor, M. R. E.: 1985, *Topological constraints associated with fast dynamo action*, J. Fluid Mech., **154**, 493–507

Magnetic flux expulsion from regions of closed streamlines is discussed in many textbooks dealing with magnetohydrodynamics. Analytical solutions for some specific cellular flows can be found for example in

Moffatt, H. K.: 1978, *Magnetic Field Generation in Electrically Conducting Fluids*, Cambridge University Press

Parker, E. N.: 1979, *Cosmical Magnetic Fields: Their Origin and their Activity*, Clarendon Press, Chap. 16

but for the first and last word on this topic, you should consult

Weiss, N. O.: 1966, *The expulsion of magnetic flux by eddies*. Proc. Roy. Soc. London Ser., A **293**, 310–328

Rhines, P. B., & Young, W. R.: 1983, *How rapidly is a passive scalar mixed within closed streamlines?*, J. Fluid Mech., **133**, 133–145

The Rhines & Young paper contains clean analytical examples of the two successive dissipative phases with characteristic timescales proportional to $R^{1/3}$ and R_m, as discussed in Sect. 2.3.4. Flux expulsion is of course not restricted to 2D flows; for a nice example in 3D see

Galloway, D. J., & Proctor, M. R. E.: 1983, *The kinematics of hexagonal magnetoconvection*, Geophys. Astrophys. Fluid Dyn., **24**, 109–136

A good recent review of the the current state of planetary magnetic field observations and models can be found in:

Stanley, S., & Glatzmaier, G. A.: 2010, *Dynamo models for planets other than Earth*, Space Sci. Rev., **152**, 617–649

On the possible symmetrization of the Saturnian magnetic field by deep-seated differential rotation, and associated dynamo-based explanations, see

Kirk, R. L., & Stevenson, D. J.: 1987, *Hydromagnetic constraints on deep zonal flow in the giant planets*, Astrophys. J., **316**, 836–846

Christensen, U. R., & Wicht, J.: 2008, *Models of magnetic field generation in partly stable planetary cores: Applications to Mercury and Saturn*, Icarus, **196**, 16–34

Stanley, S.: 2010, *A dynamo model for axisymmetrizing Saturn's magnetic field*, Geophys. Res. Lett., **37**, L05201

An insightful discussion of the symmetrization process in more general terms is that of

Rädler, K.-H.: 1986, *On the effect of differential rotation on axisymmetric and nonaxisymmetric magnetic fields of cosmic bodies*, in *Plasma Astrophysics*, Guyenne, T. D., & Zeleny, L. M., eds., ESA Special Publication, 251, Joint Varenna-Abastumani International School and, Workshop, 569–574

On anti-dynamo theorems, see

Cowling, T. G.: 1933, *The magnetic field of sunspots*, Mon. Not. Roy. Astron. Soc., **94**, 39–48

Bullard, E., & Gellman, H.: 1954, *Homogeneous dynamos and terrestrial magnetism*, Phil. Trans. Roy. Soc. London Ser., A, **247**, 213–278
Zel'dovich, Y. B.: 1956, *The magnetic field in the two-dimensional motion of a conducting turbulent fluid*, Zhurnal Eksperimentalnoi i Teoreticheskoi Fiziki, **31**, 154–156, in Russian
Zel'dovich, Y. B., & Ruzmaikin, A. A.: 1980, *The magnetic field in conducting fluid in two-dimensional motion*, Zhurnal Eksperimentalnoi i Teoreticheskoi Fiziki, **78**, 980–986, in Russian

as well as pages 113-ff and 538-ff, respectively, of the books by Moffatt and Parker listed above. English translations of the last two papers are also reprinted in

Ostriker, J. P., Barenblatt, G. I., & Sunyaev, R. A.: 1992, *Selected Works of Yakov Borisovich Zeldovich. Volume 1: Chemical Physics and Hydrodynamics*., Princeton University Press

The mathematical aspects of fast dynamo theory are discussed at length in the book of

Childress, S., & Gilbert, A. D.: 1995, *Stretch, Twist, Fold: The Fast Dynamo*, Springer

although the reader prefering a shorter introduction might want to first work through the three following review articles:

Childress, S.: 1992, *Fast dynamo theory*, in *Topological Aspects of the Dynamics of Fluids and Plasmas*, Moffatt, H., Zaslavsky, G. M., Compte, P., & Tabor, M., eds., Kluwer Academic, 111–147
Soward, A. M.: 1994, *Fast dynamos, in Lectures on Solar and Planetary Dynamos*, Proctor, M. R. E., & Gilbert, A. D., eds., Cambridge University Press, 181–218
Gilbert, A. D.: 2003, *Dynamo theory*, in *Handbook of Mathematical Fluid Dynamics*, ed. S. Frielander & D. Serre, Vol. 2, Elsevier Science, 355–441

On the Roberts cell dynamo, see Chapter 5 of the Childress & Gilbert book cited above, as well as

Roberts, G. O.: 1972, *Dynamo action of fluid motions with two-dimensional periodicity*, Phil. Trans. Roy. Soc. London Ser., A **271**, 411–454
Soward, A. M.: 1987, *Fast dynamo action in a steady flow*, J. Fluid Mech., **180**, 267–295

The scaling relations given by Eqs. (2.68)–(2.69) are derived in the second of these papers. On fast dynamo action in the CP flow, begin with:

Galloway, D. J., & Proctor, M. R. E.: 1992, *Numerical calculations of fast dynamos in smooth velocity fields with realistic diffusion*, Nature **356**, 691–693
Ponty, Y., Pouquet, A., & Sulem, P. L.: 1995, *Dynamos in weakly chaotic two-dimensional flows*, Geophys. Astrophys. Fluid Dyn., **79**, 239–257
Cattaneo, F., Kim, E.-J., Proctor, M., & Tao, L.: 1995, *Fluctuations in quasi-two-dimensional fast dynamos*, Phys. Rev. Lett., **75**, 1522–1525

The discussion in Sect. 2.6.3 follows closely that in the Cattaneo et al. (1995) paper, and the discussion of nonlinear effects in the CP flow is largely inspired from

Cattaneo, F., Hughes, D. W., & Kim, E.-J.: 1996, *Suppression of chaos in a simplified nonlinear dynamo model*, Phys. Rev. Lett., **76**, 2057–2060

but on this topic see also

Mininni, P. D., Ponty, Y., Montgomery, D. C., Pinton, J.-F., Politano, H., & Pouquet, A.: 2005, *Dynamo regimes with a nonhelical forcing*, Astrophys. J., **626**, 853–863

The mathematically inclined reader wishing to delve deeper into the theorems for fast dynamo action mentioned in Sect. 2.6 will get a solid and character building workout out of

Vishik, M. M.: 1989, *Magnetic field generation by the motion of a highly conducting fluid*, Geophys. Astrophys. Fluid Dyn., **48**, 151–167

Klapper, I., & Young, L. S.: 1995, *Rigorous bounds on the fast dynamo growth rate involving topological entropy*, Comm. Math. Phys., **173**, 623–646

On small-scale dynamo action in three-dimensional thermally-driven convective turbulence, see, e.g.,

Cattaneo, F.: 1999, *On the origin of magnetic fields in the quiet photosphere*, Astrophys. J. Lett., **515**, L39–L42
Cattaneo, F., Emonet, T., & Weiss, N.: 2003, *On the interaction between convection and magnetic fields*, Astrophys. J., **588**, 1183–1198
Stein, R. F., & Nordlund, Å.: 2006, *Solar small-scale magnetoconvection*, Astrophys. J., **642**, 1246–1255
Vögler, A., & Schüssler, M.: 2007, *A solar surface dynamo*, Astron. & Astrophys., **465**, L43–L46

http://www.springer.com/978-3-642-32092-7

Solar and Stellar Dynamos
Saas-Fee Advanced Course 39 Swiss Society for Astrophysics and Astronomy
Charbonneau, P. - Steiner, O. (Ed.)
2013, XVI, 240 p., Hardcover
ISBN: 978-3-642-32092-7